Chemical Engineering Research and Design 223 (2025) 263–279

Contents lists available at ScienceDirect

Chemical Engineering Research and Design

journal homepage: www.elsevier.com/locate/cherd

An optimisation framework for minimising power consumption, dead volume, and shear rate of mixing tanks containing shear-thinning fluids utilising CFD

Liam Merrick Boston, Jos Derksen, Aniruddha Majumder *

School of Engineering, University of Aberdeen, Aberdeen, AB24 3UE, United Kingdom

ARTICLE INFO

Keywords:
Anaerobic digestion
Computational fluid dynamics
Design of experiments
Helical-ribbon impeller
Lattice Boltzmann method
Mixing tank optimisation
Non-Newtonian shear-thinning power-law fluid

ABSTRACT

A hydrodynamic model of a laminar mixing tank containing a shear-thinning power-law fluid stirred by a helical ribbon impeller is created using the Lattice Boltzmann Method and used to train regression models to predict power number, percentage of dead volume, and shear rate statistics. A Reduced Gradient Algorithm is used to maximise a Composite Desirability Function, composed of the regression models, to optimise impeller geometry for selected flow behaviour indices following a Design of Experiments methodology. The regression models are trained on sixty simulations, and validated on eight separate simulations. The range of deviation between regression models and each output response are as follows: impeller power number = 0.047 % to 18 %, percentage of tank dead volume = 0.34 % to 18 %, average shear rate = 0.56 % to 9.0 %, maximum shear rate = 0.46 % to 11 %, and standard deviation of shear rate = 0.69 % to 5.5 %. This is found to be an efficient methodology for optimising mixing conditions, when only a hydrodynamic model is available.

1. Introduction

Mixing is a process ubiquitous across a breadth of chemical industries, being a key design feature of reactors as used in the fermentation (Zhang et al., 2023), waste water treatment (López-Jiménez et al., 2015), and pharmaceutical (Alberini et al., 2024) industries. Mixing plays a critical role in reactor performance, ensuring even mixing to reduce dead volume formation, reactor short-circuiting, and minimise local variations in reactant concentrations (Paul et al., 2003). Mixing is also responsible for a large proportion of energy consumption (Singh et al., 2019; Dapelo et al., 2023). As such, over the years there have been consistent efforts to optimise mixing conditions, such that the desired mixing state can be achieved with minimal energy input (Mihailova et al., 2018; Tsui and Hu, 2011; Singh et al., 2021; Yao et al., 2023). This work is focused on optimising the mixing tank in the context of anaerobic digestion where the content of the tank is modelled by shear-thinning power-law fluids.

Many CFD methods exist, each with their own inherent strengths and weaknesses. In the context of mixing tank simulation, particularly in the realm of fermentation processes, the most relevant numerical methods are the finite volume method (FVM) (López-Jiménez et al., 2015; Meister et al., 2018; Mihailova et al., 2018; Neuner et al., 2024), the finite element method (FEM) (Huang et al., 2018; Soheel et al., 2023), the lattice Boltzmann method (LBM) (Landry et al., 2004; Dapelo et al., 2019), and smoothed-particle hydrodynamics (SPH) (Robinson and Cleary, 2012; Rezavand et al., 2019).

In recent years, it has been shown that LBM (Krüger et al., 2017) can be significantly more efficient than the prevalent FVM and FEM (Dapelo et al., 2023). Derksen (2018) simulates stirring of spherical particles suspended in a Newtonian fluid within a cubic tank using an in-house developed LBM solver. Dapelo et al. (2019) use LBM to simulate a lab-scale gas-mixed anaerobic digester with a volume of 4 L where a shear-thinning power-law liquid is modelled as well as rigid spherical gas bubbles. A rheology similar to the manure slurry of Landry et al. (2004) is used for total solids concentration of 2.5% and 5.4% by mass. Dapelo et al. (2023) then apply a similar model utilising OpenLB (Kummerländer et al., 2024) to an industrial scale gas-mixed anaerobic digester, with a volume of roughly 2570 m^3. An increase in computational efficiency of over 1000 times is claimed over an analogous FVM model. The authors note the limitations of this comparison, and advise against the use of this figure as a strict benchmark, but rather that it can be used as a broad argument as to the efficiency of LBM on parallel hardware. Eibl et al. (2020) give a comprehensive guide on bioreactor modelling using LBM, incorporating hydrodynamics, two-phase flow, mass transport of chemical species, and energy transport.

* Corresponding author.
E-mail addresses: l.boston.19@abdn.ac.uk (L.M. Boston), jderksen@abdn.ac.uk (J. Derksen), a.majumder@abdn.ac.uk (A. Majumder).

https://doi.org/10.1016/j.cherd.2025.09.025
Received 7 July 2025; Received in revised form 9 September 2025; Accepted 15 September 2025
Available online 23 September 2025

While CFD can be an excellent tool for obtaining a detailed description of a system, complex models can take large amounts of time to simulate. The mixing tank simulations of this project typically take around a day to complete. Although, in principle, numerous CFD simulations can be run to fully map the parameter space of a response, this is computationally very expensive. This can be alleviated by the use of surrogate modelling, whereby relatively simple models are inferred from simulation data. In what follows, a selection of recent optimisation studies are summarised.

Tsui and Hu (2011) optimise the geometry of a single-blade helical ribbon impeller agitated mixture with the goal of increasing circulating flow rate, and decreasing mixing time and power consumption. Mihailova et al. (2018) perform an optimisation study examining the mixing performance and energy consumption as a function of the geometry of 98 innovative impeller designs, which combine features of double-blade helical ribbon impellers, anchor impellers, and axial screws. Singh et al. (2021) first investigate the effect of the impeller speed of a single helical ribbon impeller on biogas production in three 5 L lab-scale reactors via experiment, then replicate this setup with CFD simulation using *ANSYS® Fluent* (ANSYS, Inc., 2023), with the k-ω turbulence model, and inspects the effect of impeller speed on the quantity of dead volume. It is found that higher speeds give a reduction of dead volume and more biogas production, but lower volatile fatty acids production, and dead volume quantity is reduced from 18% to 17% to 2%. Mao et al. (2021) design a horizontal reactor with inner and outer helical ribbons for anaerobic digestion of high-solids horticultural waste, using CFD as an initial step before validating via experiment. Energy efficiency through intermittent mixing is investigated. Yao et al. (2023) use CFD to model a baffled mixing tank with a dual pitched-blade impeller, which mixes a suspension of water and particles. 80 simulations are used to train a surrogate Kriging regression model and optimisation is performed on the surrogate model using non-dominated sorting genetic algorithm II, with competing objectives of power consumption and suspension uniformity. Chen et al. (2019) investigate a variety of propeller, pitched-blade, frame, and helical ribbon impeller (HRI) configurations at 100 rpm, 150 rpm and 300 rpm for the production of bacterial nanocellulose, concluding that helical ribbon and coaxial propellers give better mixing, and better yield of bacterial nanocellulose. Lebranchu et al. (2017) investigate the effect of shear stress and impeller design on biogas production, and examines impeller speeds of 10 rpm, 50 rpm and 90 rpm at generalised Reynolds numbers of 1.7, 25.2 and 67.5. It is concluded that HRI produces 50% more biogas than a Rushton impeller while consuming less energy. The key shear statistic is maximum shear stress. Wu et al. (2022) use *Siemens Simcenter STAR-CCM+* (Siemens Digital Industries Software, 2021b) to model the hydrodynamics and advection–diffusion of a passive scalar within a baffled mixing tank, operating at a Reynolds number of around 10^5 with a Rushton impeller and pitched-blade impeller. Using *Siemens HEEDS* (Siemens Digital Industries Software, 2021a) design exploration software, the multi-objective SHERPA optimisation algorithm is used to produce optimised designs for minimising mixing time and power consumption by altering impeller diameter, the number of blades of the Rushton impeller, and the blade pitch of the pitched-blade impeller.

The overall aim of this work is to propose an efficient framework to optimise the mixing conditions within mixing tanks, containing highly viscous, shear-thinning liquids, using a computational fluid dynamics approach. The identified knowledge gaps and the associated novelties/contributions of this work are listed below:

- Optimal conditions leading to a well-mixed system is something that few studies address for anaerobic digesters with solids concentrations above 10%. This can lead to improved reactor efficiency, allowing a smaller tank volume to be used compared to operating at lower solids concentrations (Battista et al., 2016; Wu, 2012; Neuner et al., 2024). This study seeks to optimise impeller geometry for a range of fluid rheologies correlating to high solids concentration fluids as found within anaerobic digesters.
- Most of the literature examining optimal mixing conditions in the context of anaerobic digestion ignores the shear rate which may damage the microorganisms above a certain value. One of the objectives of the optimisations carried out in this work is to limit maximum shear rate.
- We are aware of only four studies that use LBM in the context of anaerobic digestion (Fortunato et al., 2018; Dapelo et al., 2019, 2020, 2023), and none of these show a stirred tank. A gap thus exists to prove the suitability of LBM for simulating such a system. This study presents LBM as an efficient and accurate hydrodynamic solver for this purpose.
- While a wealth of studies employing a range of optimisation strategies exist for various mixing systems, most studies examining HRI design use a basic one-variable-at-a-time approach (Tsui and Hu, 2011; Singh et al., 2021; Mao et al., 2021; Delaplace et al., 2000a; Lebranchu et al., 2017), as opposed to an extensive design of experiment (DoE) approach. None include a preliminary screening stage, and none simultaneously examine the competing objectives of power consumption, percentage of dead volume, and shear rate minimisation. This provides an opportunity for a study that introduces the systematic optimisation of an HRI using a DoE approach, subject to the minimisation of the mentioned responses, which this study investigates.

A description of the remaining contents of this article follows. Section 2 discusses the methodologies used in this project, introducing the models relevant to stirred tank hydrodynamics with non-Newtonian rheology, and discussing the adopted optimisation framework. Section 3 details the studies undertaken to verify and validate the LBM hydrodynamic model used for simulating mixing tank systems, before applying and validating the optimisation framework. Section 4 summarises the main achievements of the project and discusses topics for future research.

2. Methods

Optimisation of impeller and tank geometry at different flow behaviour indices for the competing objectives of dead volume and power consumption minimisation use a design of experiments (DoE) response surface methodology (RSM) derived framework to form polynomial surrogate models from hydrodynamic LBM simulations, and the proprietary reduced gradient algorithm (RGA) of *Minitab® (20.3)* (Minitab, LLC., 2021) is used to maximise composite desirability functions (CDF) utilising these models.

2.1. Stirred tank flow modelling

All models used assume laminar flow (justified by the high fluid viscosity which dampens inertial effects), and an incompressible single-phase fluid. Gravity effects on the fluid are assumed to be negligible since the Reynolds number is low (Re < 300) (Rushton et al., 1950; Paul et al., 2003), thus the Froude number is irrelevant as no significant disturbances will be present on the free surface of the tank. To obtain the transient velocity field and hydrodynamics of the fluid within the mixing tank, the following continuity and momentum equations are solved respectively (Bird et al., 2015):

$$\nabla \cdot \mathbf{u} = 0\,, \tag{1}$$

$$\rho\left(\frac{\partial \mathbf{u}}{\partial t} + \mathbf{u}\cdot\nabla\mathbf{u}\right) = -\nabla p + \nabla\cdot\boldsymbol{\tau} + \mathbf{F}\,, \tag{2}$$

with fluid density ρ (kg m^{-3}) a constant, time t (s), fluid velocity vector $\mathbf{u}$ (m s^{-1}), pressure p (Pa), and viscous stress tensor $\boldsymbol{\tau}$ (Pa). The specific body force applied to the fluid $\mathbf{F}$ (N m^{-3}) ensures the no-slip boundary condition is met on the surface of the impeller and tank side-wall via an immersed boundary method (IBM) (Goldstein et al., 1993; Derksen and Van den Akker, 1999); the details of this are discussed in Section 2.1.2.

2.1.1. Non-Newtonian rheology

The fluid is modelled as non-Newtonian shear-thinning, with the local apparent dynamic viscosity η (Pa s) obeying one of two rheological models: either the power-law rheological model (de Waele, 1923; Ostwald, 1925) for Section 3.2, or the Herschel–Bulkley model (Ford et al., 2006) for Section 3.1.

The power-law model reads

$$\eta = k\dot{\gamma}^{n-1} \qquad \text{at} \quad \dot{\gamma}_{\min} < \dot{\gamma} < \dot{\gamma}_{\max}\,, \tag{3}$$

with flow consistency index k (Pa s^n), flow behaviour index n (dimensionless), and local shear rate $\dot{\gamma}$ (s^{-1}). Power-law fluids exhibit shear-thinning ($n < 1$) or shear-thickening ($n > 1$) behaviour over a certain range of $\dot{\gamma}$. To accurately reproduce their behaviour, and avoid numerical instabilities at extreme values of $\dot{\gamma}$, the power law is truncated such that, for shear-thinning fluids,

$$\eta = \mu_{\min} \qquad \text{at} \quad \dot{\gamma} \geq \dot{\gamma}_{\max}\,, \tag{4}$$

$$\eta = \mu_{\max} \qquad \text{at} \quad \dot{\gamma} \leq \dot{\gamma}_{\min}\,. \tag{5}$$

The magnitude of the symmetrical strain rate tensor $\boldsymbol{\epsilon}$ (s^{-1}) allows $\dot{\gamma}$ to be expressed as (Bird et al., 2015)

$$\dot{\gamma} = \sqrt{\frac{1}{2}\boldsymbol{\epsilon} : \boldsymbol{\epsilon}} = \sqrt{\frac{1}{2}\left(\epsilon_{xx}^2 + \epsilon_{yy}^2 + \epsilon_{zz}^2\right) + \epsilon_{xy}^2 + \epsilon_{xz}^2 + \epsilon_{yz}^2}\,, \tag{6}$$

itself defined as

$$\boldsymbol{\epsilon} = \nabla\mathbf{u} + (\nabla\mathbf{u})^{\mathrm{T}} = \begin{bmatrix} 2\frac{\partial u_x}{\partial x} & \frac{\partial u_x}{\partial y} + \frac{\partial u_y}{\partial x} & \frac{\partial u_x}{\partial z} + \frac{\partial u_z}{\partial x} \\ \frac{\partial u_y}{\partial x} + \frac{\partial u_x}{\partial y} & 2\frac{\partial u_y}{\partial y} & \frac{\partial u_y}{\partial z} + \frac{\partial u_z}{\partial y} \\ \frac{\partial u_z}{\partial x} + \frac{\partial u_x}{\partial z} & \frac{\partial u_z}{\partial y} + \frac{\partial u_y}{\partial z} & 2\frac{\partial u_z}{\partial z} \end{bmatrix}. \tag{7}$$

For validation of the non-Newtonian hydrodynamic model in Section 3.1, the fluid modelled is a xanthan gum solution (Prajapati and Ein-Mozaffari, 2009), using the Herschel–Bulkley yield-stress rheology model. Since viscosity tends towards infinity as shear rate tends towards zero for shear-thinning fluids, a modified form of the Herschel–Bulkley equation (Ford et al., 2006) is used to prevent numerical instability, where the substance acts as a very viscous fluid at low shear rates instead of as a solid. Here, the apparent dynamic viscosity is equal to a constant yielding dynamic viscosity μ_0 (Pa s) until the shear rate rises above a critical shear rate $\dot{\gamma}_c$ (s^{-1}), defined by yield shear stress τ_y (Pa) over μ_0, such that

$$\dot{\gamma}_c = \frac{\tau_y}{\mu_0}\,, \tag{8}$$

$$\eta = \mu_0 \qquad \text{at} \quad \dot{\gamma} \leq \dot{\gamma}_c\,, \tag{9}$$

$$\eta = \frac{\tau_y + k\left[\dot{\gamma}^n - \left(\frac{\tau_y}{\mu_0}\right)^n\right]}{\dot{\gamma}} \qquad \text{at} \quad \dot{\gamma} > \dot{\gamma}_c\,. \tag{10}$$

As τ_y and μ_0 are empirical constants for a specific fluid, they are converted from SI units to lattice units as described in the following Section 2.1.2.

2.1.2. Lattice Boltzmann method for hydrodynamics

The LBM of Somers and Eggels (Somers, 1993; Eggels and Somers, 1995) is used here as employed by Derksen (Derksen and Van den Akker, 1999; ten Cate et al., 2002; Derksen, 2018) to solve Eqs. (1) and (2). Full details are available in Section 3.1.2 of Boston (2025). As all operations are either local or near-neighbour, the algorithm lends itself very well to parallelisation (Dapelo et al., 2023).

The simulation domain is a cuboid completely filled with a single-phase fluid discretised by a regular cubic lattice with spacing Δx (m). Eqs. (1) and (2) are solved at the nodes of this lattice. Coordinates, referred to as control points, represent the surfaces of the side tank walls and the impeller. These control points do not coincide with the lattice, and are only used to enforce boundary conditions.

A free-slip boundary condition is employed at the top of the domain, and no-slip conditions are used at the other domain limits. To enforce the no-slip condition on the impeller and tank wall surfaces, the IBM of Goldstein et al. (1993) is utilised herein as per Derksen and Van den Akker (1999) and ten Cate et al. (2002). This applies a body force to the lattice nodes adjacent to the control points to enforce the no-slip condition, and is remarkably flexible for a range of geometries with little in the way of complex meshing required — simply a series of points on the boundary surface.

In IBMs, the spacing between the control points typically lies between $0.5\,\Delta x$ to $1.5\,\Delta x$ (Krüger et al., 2017; Xiao et al., 2020). Too fine a spacing results in instability, while too large a spacing allows fluid to permeate the boundary. From preliminary simulations, it is found that a spacing of Δx between the control points on the tank wall in the vertical (z) direction and $0.8\,\Delta x$ along the circumference works. The tank ends $0.5\,\Delta x$ from the top and bottom of domain, and lies $2.5\,\Delta x$ from the sides. The impeller geometry is created in *SOLIDWORKS® 2021 Education Edition* (Dassault Systèmes SolidWorks Corporation, 2021), and is exported to *ANSYS® Fluent Meshing 2022 R1* (ANSYS, Inc., 2022) where impeller control points are generated from an unstructured grid of triangular elements, with points spaced about $0.8\,\Delta x$ apart. The impeller shaft stops and is capped $0.5\,\Delta x$ from the domain top.

It is convenient in LBM to use lattice units as opposed to SI units. In lattice units, one length unit Δx is the lattice length, i.e. the distance between adjacent lattice nodes, one mass unit M is the amount of mass contained within a cube with sides of length $1\,\Delta x$, and one time unit Δt is equal to one time step, i.e. one iteration of the LBM algorithm. Every time step Δt, particles move to neighbouring lattice sites. To translate between SI units and lattice units, the conversion factors C_l (m Δx^{-1}), C_m (kg M^{-1}), and C_t (s Δt^{-1}) are derived for base units of length, mass, and time respectively. In the context of simulating a mixing tank, these may be defined as

$$C_l = \frac{d_{\mathrm{imp,SI}}}{d_{\mathrm{imp,lu}}}\,, \tag{11}$$

$$C_m = \frac{\rho_{\mathrm{SI}}}{\rho_{\mathrm{lu}}} \cdot C_l^3\,, \tag{12}$$

$$C_t = \frac{N_{\mathrm{lu}}}{N_{\mathrm{SI}}}\,, \tag{13}$$

where subscript "SI" represents a quantity in SI units, and subscript "lu" denotes a quantity in lattice units. Impeller diameter d_{imp} (m) is used for length conversion, ρ multiplied by C_l cubed for mass conversion, and impeller rotational frequency N (rev s^{-1}) for time conversion. To convert τ_y and μ_0 of the Herschel–Bulkley rheology model (Eq. (10)), and k of both the Herschel–Bulkley and power-law models (Eq. (3)), from SI to lattice units, Eqs. (11)–(13) are used as

$$\tau_{y,\mathrm{lu}} = \tau_{y,\mathrm{SI}} \cdot \frac{C_l C_t^2}{C_m}\,, \tag{14}$$

$$\mu_{0,\mathrm{lu}} = \mu_{0,\mathrm{SI}} \cdot \frac{C_l C_t}{C_m}\,, \tag{15}$$

$$k_{\mathrm{lu}} = k_{\mathrm{SI}} \cdot \frac{C_l}{C_m C_t^{n-2}}\,. \tag{16}$$

Eqs. (1) and (2) are solved in the limit of low Mach number Ma (dimensionless) (Ma < 0.1), with Ma defined as

$$\mathrm{Ma} = \frac{|\mathbf{u}|_{\max}}{c_s}\,, \tag{17}$$

where both maximum fluid velocity vector magnitude $|\mathbf{u}|_{\max}$ and speed of sound c_s are in lattice units. For the LBM scheme used here, $c_s^2 = 1/2\,\Delta x^2\,\Delta t^{-2}$ (Somers, 1993; Eggels and Somers, 1995; ten Cate et al., 2002), as opposed to $1/3\,\Delta x^2\,\Delta t^{-2}$ in more common schemes (Krüger et al., 2017).

2.1.3. Mixing tank hydrodynamics

The impeller Reynolds number Re (dimensionless) gives the ratio of inertial to viscous forces in the fluid, with laminar mixing up to a Re of around 10 to 100 (Paul et al., 2003) depending upon geometry and fluid properties. For a Newtonian fluid, this is defined as

$$\mathrm{Re} = \frac{N d_{\mathrm{imp}}^2}{\nu}, \tag{18}$$

with global constant ν; however, for a non-Newtonian fluid, a ν representative of the whole mixture must be chosen. So that Re can be used as an input parameter for simulations, the Metzner–Otto correlation (Metzner and Otto, 1957) is used to predict the average shear rate $\dot{\gamma}_{\mathrm{avg}}$ (s^{-1}),

$$\dot{\gamma}_{\mathrm{avg}} = K_{\mathrm{S}} N, \tag{19}$$

which is used with ρ in Eq. (3) to give the apparent kinematic viscosity ν_{app} ($\mathrm{m}^2\ \mathrm{s}^{-1}$) of the mixture. Eq. (19) states that the average shear rate an impeller imposes upon a non-Newtonian fluid is proportional to N, with a constant of shear K_{S}, however over what volume of fluid adjacent to the impeller this relation applies to is not well-defined. Further, the relations used to calculate K_{S} for a certain mixing system is widely debated, with some arguing it is purely a function of impeller and tank geometry, and others claiming it also depends upon rheology, marginally increasing with an increase in flow behaviour index n for shear-thinning fluids, leading to a number of relations for K_{S} for any given impeller (Shekhar and Jayanti, 2003; Delaplace et al., 2000b). Ramírez-Muñoz et al. (2017) seek to address this issue, presenting a method to determine K_{S} using laminar steady-state non-Newtonian CFD simulations, and investigate the region around a Rushton impeller at which the Metzner–Otto correlation applies. They determine this region to be the volume of fluid swept by the impeller blades and conclude that fluid rheology has very little influence in the value of K_{S}. Guadarrama-Pérez et al. (2020) then use this method to determine K_{S} for high-shear ring-style impellers mixing a non-Newtonian fluid in the laminar regime and subsequently evaluate the hydrodynamic performance of the impeller. They again conclude minimal influence of fluid rheology upon K_{S}.

The use of Eq. (19) allows a generalised impeller Reynolds number Re_{g} to be found for a power-law fluid as

$$\mathrm{Re}_{\mathrm{g}} = \frac{N d_{\mathrm{imp}}^2}{\nu_{\mathrm{app}}} = \frac{\rho N d_{\mathrm{imp}}^2}{k \dot{\gamma}_{\mathrm{avg}}^{n-1}} = \frac{\rho N d_{\mathrm{imp}}^2}{k \left(K_{\mathrm{S}} N\right)^{n-1}}. \tag{20}$$

For a Herschel–Bulkley fluid, the definitions

$$\nu_{\mathrm{app}} = \frac{\tau}{\dot{\gamma}_{\mathrm{avg}} \rho}, \tag{21}$$

$$\tau = \tau_{\mathrm{y}} + k \dot{\gamma}_{\mathrm{avg}}^{n}, \tag{22}$$

are used (Prajapati and Ein-Mozaffari, 2009), giving

$$\mathrm{Re}_{\mathrm{g}} = \frac{\rho N^2 d_{\mathrm{imp}}^2 K_{\mathrm{S}}}{\tau_{\mathrm{y}} + k \left(K_{\mathrm{S}} N\right)^{n}}. \tag{23}$$

The relations for K_{S} used here for anchor and helical ribbon impellers respectively are those of (Shamlou and Edwards, 1989, 1985),

$$K_{\mathrm{S,anc}} = 33 - 172 \frac{c_{\mathrm{side}}}{d_{\mathrm{tank}}}, \tag{24}$$

$$K_{\mathrm{S,HRI}} = 34 - 144 \frac{c_{\mathrm{side}}}{d_{\mathrm{tank}}}, \tag{25}$$

with tank diameter d_{tank} (m), and impeller side clearance c_{side} (m) defined as

$$c_{\mathrm{side}} = \frac{d_{\mathrm{tank}} - d_{\mathrm{imp}}}{2}. \tag{26}$$

Impeller power consumption P (W) allows impeller power number Po (dimensionless) to be calculated as a function of N, ρ and d_{imp} as

$$\mathrm{Po} = \frac{P}{\rho N^3 d_{\mathrm{imp}}^5}. \tag{27}$$

Given Po, P can be found through two methods — via the torque T (N m) of the impeller, which represents the power input to the system by the impeller, and via the total viscous dissipation within the fluid E_{V} (W), which represents the energy lost per unit time in the system due to internal fluid friction (Bird et al., 2015). These should be equal assuming no other energy sources or sinks, and that an equilibrium is reached between energy input and energy dissipation, thus serving as a useful method of verifying the hydrodynamic model. $P(T)$ is found from

$$P(T) = 2\pi N T, \tag{28}$$

while $P\left(E_{\mathrm{V}}\right)$ is found by integrating the local viscous dissipation rate over the entire fluid volume (Bird et al., 2015),

$$P\left(E_{\mathrm{V}}\right) = -\int_V \boldsymbol{\tau} : \nabla \mathbf{u} \mathrm{d}V, \tag{29}$$

with $\boldsymbol{\tau}$ the viscous stress tensor (Pa)

$$\boldsymbol{\tau} = -\eta \boldsymbol{\epsilon}. \tag{30}$$

By replacing η in Eq. (30) with a rheological model such as Eq. (3), and with $\boldsymbol{\epsilon}$ defined previously in Eqs. (7), (29) can be rewritten as

$$P\left(E_{\mathrm{V}}\right) = \int_V k \dot{\gamma}^{n-1} \left[\frac{1}{2}\left(\epsilon_{xx}^2 + \epsilon_{yy}^2 + \epsilon_{zz}^2\right) + \epsilon_{xy}^2 + \epsilon_{xz}^2 + \epsilon_{yz}^2\right] \mathrm{d}V. \tag{31}$$

Components of $\boldsymbol{\epsilon}$ are found from moments of the distribution function by Eq. (7) via Eq. (A.5). They can also be found from approximations of velocity gradients, but preliminary simulations (Boston, 2025) have shown this method to not align as close to experimental values (Bertrand, 1983; Mokhefi et al., 2022), presumably due to inaccuracies introduced by estimating velocity gradients. Appendix A describes how to obtain $\boldsymbol{\epsilon}$ directly from the distribution function.

Mixing quality in the hydrodynamic model is determined by the percentage of dead volume ϕ_{dead} (%) in the tank. Common definitions of a dead volume in literature are as a region of fluid with an upward velocity lower than the Stokes' settling velocity of a particle of certain size and density (Karim et al., 2004) resulting in sedimentation, or with a speed lower than 5% of the maximum fluid speed in the tank (Vesvikar et al., 2005). This value of 5% seems to be arbitrarily chosen, and no justification is given for the choice of maximum fluid speed as the benchmark. In this study, impeller tip speed u_{tip} ($\mathrm{m\ s}^{-1}$) is used as the benchmark since it is a well-defined input parameter, so the volume surrounding a fluid node at position $\mathbf{x}$, and at time t, is considered a dead volume if

$$|\mathbf{u}(\mathbf{x}, t)| < 0.05 u_{\mathrm{tip}}. \tag{32}$$

Simulations are run until a pseudo-steady state is reached, and for a period of time after this to allow for accurate long-term time-averaging of the output responses of interest (Po, ϕ_{dead}, shear rate statistics etc.). The system is deemed to be at a pseudo-steady state when the short-term time-averaged output responses reach steady values. A pseudo-steady state in this system is reached after about 3 impeller revolutions.

Short-term time-averaging occurs over periods of half an impeller revolution, while long-term time averaging occurs from the point at which a pseudo-steady state is reached until the end of the simulation. The final values reported are long-term time-averages. To obtain the time-averaged values, variables are sampled every $100\,\Delta t$. Preliminary simulations as described in Section 3.1 have shown this sampling frequency to resulting in a deviation below 0.5% compared to sampling every time step, and vastly reduces the quantity of operations required (Boston, 2025).

2.2. Optimisation framework

A general optimisation framework is presented to find optimal combinations of impeller and tank geometry parameters at different

flow behaviour indices, at a constant Re_g, for the competing objectives of power consumption, dead volume, and shear rate minimisation. This follows a DoE RSM approach (Box and Wilson, 1951; Box et al., 2005; Antony, 2014; Montgomery, 2019), with the use of *Minitab®(20.3)* (Minitab, LLC., 2021). This procedure can be followed to identify the most important input parameters affecting a series of output responses, then suggest optimal input configurations utilising surrogate models to achieve output goals, while minimising the number of experiments or simulations required. A summary of this framework follows:

1. Screening of input parameters: a definitive screening design (DSD) (Jones and Nachtsheim, 2013) identifies the key input parameters affecting a selection of output responses.
2. Training of surrogate models: Latin hypercube sampling (LHS) (McKay et al., 1979) generates combinations of input parameter values for a series of simulations. The results of these simulations form training data from which 2nd order polynomial regression equations are generated to be used as surrogate models during optimisation.
3. Validation of surrogate models: the results of additional simulation runs are set aside as validation data to test the predictive ability of the surrogate models upon combinations of input parameters from which they have not been trained.
4. Optimisation of output responses: a proprietary RGA (Minitab, LLC., 2021) performs a multi-objective optimisation, with the CDF (Derringer and Suich, 1980; Derringer, 1994) used as the objective function. The surrogate models are used in the CDF.

An illustration of the framework is provided as a flow chart in Fig. 1.

A DoE approach is vital to optimise multiple parameters of a complex, non-linear system, such as a mixing tank, to minimise experimental costs and computational time, but still obtain high-quality data that can accurately infer relations between input parameters and output responses. A description of the framework summarised above now follows.

2.2.1. Definitive screening design

First, input parameters are screened to determine which are the most influential on the output responses of interest by running simulations with various input values and calculating output responses. An experimental design determines how many simulations to run, and the values of input parameters to use for each simulation. Choosing an appropriate experimental design ensures efficient use of resources. DSD (Jones and Nachtsheim, 2013) is a factorial method that uses relatively few experiments to determine relations between inputs and outputs. The qualitative inputs have two levels (− and +), while the quantitative inputs have three levels (−, 0, and +).

Simulations are run with inputs according to a DSD table (provided in Section 1 of the supplementary material), outputting time-averaged values of impeller power number, percentage of dead volume, maximum shear rate, volume-averaged shear rate, and standard deviation of shear rate within the fluid. RSM (Box and Wilson, 1951; Box et al., 2005) maps the surface of output responses via polynomial equations describing the relations between inputs and outputs

The RSM implemented here constructs 2nd order polynomials with interaction terms for each output response using a forward stepwise regression approach. In this approach, starting from a model with no terms, the most significant variables are added, and least significant variables are removed during each step systematically for p-values ≥ 0.05. The p-value represents the probability of failing to reject the null-hypothesis.

Next, the corrected Akaike's information criterion (AICc) (Hurvich and Tsai, 1989), is utilised to obtain a measure of the quality for the new model as

$$\mathrm{AICc} = -2\ln(\mathcal{L}) + 2a + \frac{2a(a+1)}{b-a-1}, \tag{33}$$

with number of coefficients a, sample size b, and likelihood function $\mathcal{L}$ (dimensionless). AICc gives a measure of the quality of a model relative to other models, with a lower value indicating a higher quality. The fraction on the right of Eq. (33) is a penalty term that penalises overfitting. This process continues until either all linear, 2nd order and interaction terms have entered the model, or a model has one degree of freedom, or no model provides a new minimum AICc after eight consecutive steps. The model with the lowest AICc is then used. A hierarchical structure is enforced (2nd order and interaction terms require relevant linear terms), with additional terms allowed to enter at each step to ensure this. An issue with stepwise regression is its tendency to overfit (Hurvich and Tsai, 1989). AICc mitigates this to some extent due to the penalty term, but care must still be taken when extrapolating outwith the range of training data.

Finally, to determine whether an input term is significant, a Pareto chart is constructed for each output (as per the results discussed in Section 3.2.1). This is a bar plot which illustrates the standardised effect of each input term in the polynomial with respect to the output. A straight line α bisecting the plot represents the threshold p-value, here set to 0.05. Any bars that fail to cross this line have an insignificant effect on the output. Being cautious to apply experience and knowledge of the system being modelled to the results of this process, input parameters can be screened and either included or discarded from subsequent analyses.

2.2.2. Surrogate modelling

Training data is generated by running mixing tank simulations. The input values are decided according to LHS (McKay et al., 1979). This is a space filling sampling method that attempts to provide equal representation for each area of the parameter space. Regression models are generated from the training data following the same forward stepwise regression approach as in the screening process described above. These regression models are then validated against separate simulation data testing their suitability as surrogate models, exploring their predictive powers by comparing the deviation between their predictions and simulation results.

2.3. Multi-objective optimisation

To find the optimal configuration of input parameters to minimise or maximise output responses, an objective function in the form of a CDF is first formed (Derringer and Suich, 1980; Derringer, 1994) using the surrogate models for each output response. Individual desirability d_i is a value between 0 to 1 measuring how well a single output response is optimised — 0 being not at all optimised, and 1 being optimal. For minimising an output, this is calculated as

$$d_i = 0 \qquad \text{for} \quad \hat{Y}_i > Y_{i,\max}, \tag{34}$$

$$d_i = \left(\frac{Y_{i,\max} - \hat{Y}_i}{Y_{i,\max} - Y_{i,\min}}\right)^{r_i} \qquad \text{for} \quad Y_{i,\min} \leq \hat{Y}_i \leq Y_{i,\max}, \tag{35}$$

$$d_i = 1 \qquad \text{for} \quad \hat{Y}_i < Y_{i,\min}, \tag{36}$$

for response i, weighted by r_i, with predicted value of response obtained by surrogate model $\hat{Y}_i$, constrained by maximum allowed response value $Y_{i,\max}$, and target response value $Y_{i,\min}$. Weighting r_i controls the rate of change of d_i with respect to $\hat{Y}_i$ as $\hat{Y}_i$ goes from $Y_{i,\min}$ to $Y_{i,\max}$, and $0 < r_i \leq 10$. $r_i = 1$ corresponds to a linear decrease of d_i with respect to $\hat{Y}_i$, $r_i < 1$ corresponds to a gradual decrease, and $r_i > 1$ corresponds to a sharp decrease; thus, a larger weighting will force a sharper decrease in d_i as $\hat{Y}_i$ moves away from its target value, affecting the composite desirability to a greater extent.

For multiple competing objectives, a composite desirability D is calculated from the geometric mean of d_i, weighted by relative importance of each response w_i:

$$D = \left[\prod \left(d_i^{w_i}\right)\right]^{\frac{1}{\sum w_i}}. \tag{37}$$

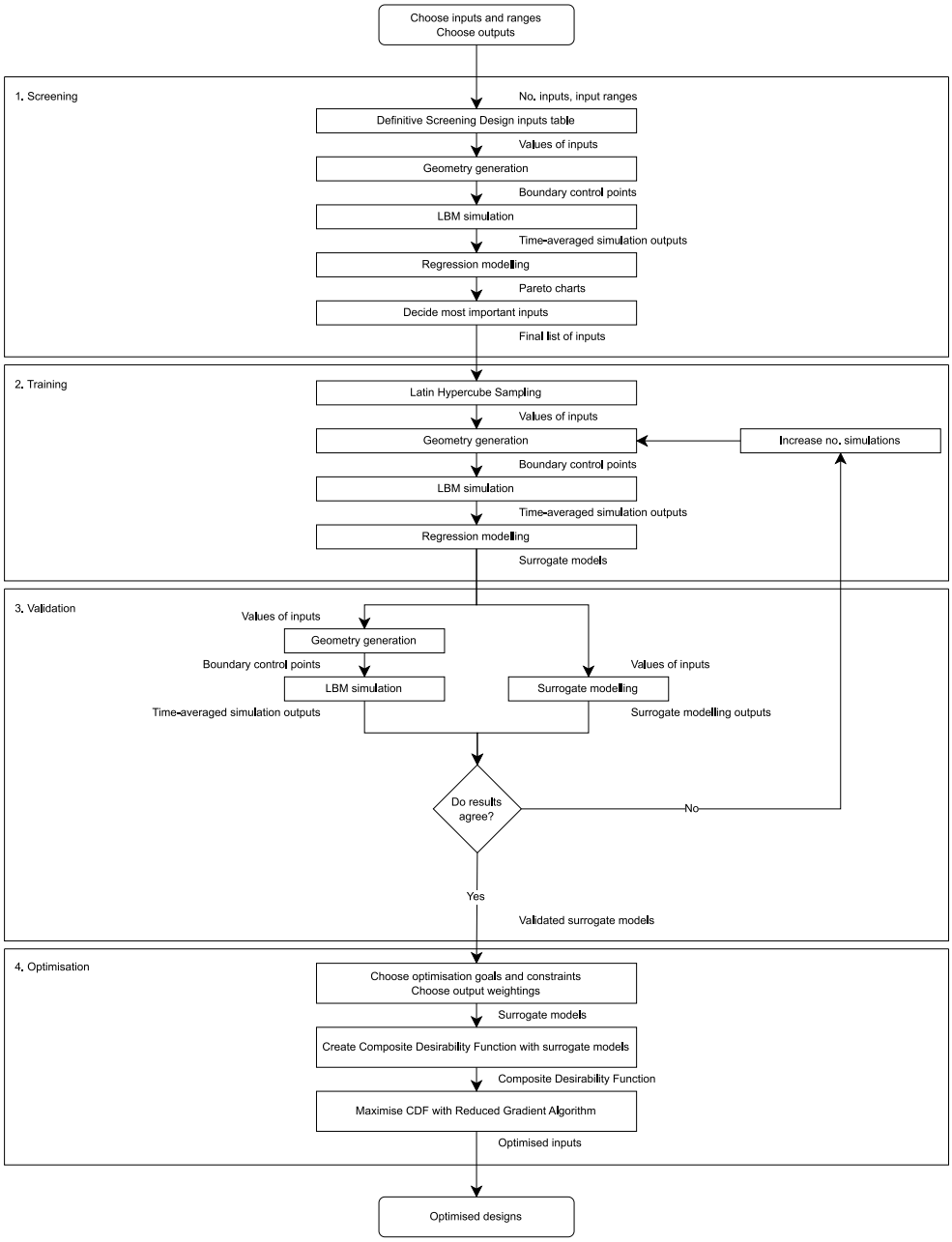

Fig. 1. Simplified flow chart of optimisation framework.

This measures how well all output responses have been optimised, also on a scale of 0 to 1. Importance w_i determines the contribution of each individual desirability to the composite desirability, and $0 < w_i < 10$.

The proprietary gradient-based technique known as theeduced gradient algorithm (RGA) (Frank and Wolfe, 1956; Lasdon et al., 1978; Rao, 2019) of commercial software *Minitab®(20.3)* (Minitab, LLC., 2021) is used to maximise the value of D. It is a fast and suitable technique to use since 2nd order polynomials are to be optimised, which will have a single global minimum or maximum.

2.4. Computer hardware specifications

LBM simulations are performed on both the supercomputing cluster Maxwell at the University of Aberdeen, running Red Hat enterprise Linux 8.6, on Intel Xeon Gold 6330 CPUs (28 C/56 T @ 2.0 GHz to 3.1 GHz), with 32 GB DDR4-3200 RAM, and an HP Z6 G4 workstation, running Ubuntu 22.04.3 LTS x86_64, on an Intel Xeon Gold 6230 CPU (20 C/40 T @ 2.1 GHz to 3.9 GHz), 4 x 32 GB DDR4-2933 RAM, and a 512 GB M.2 SSD. The most demanding simulations in Section 3.2.2 take around 26 h to complete on Maxwell, each running on 4 cores with under 4 GB of RAM.

3. Results and discussion

Presented here is a selection of results with accompanying discussions. First, the mixing tank model is validated against literature data for a non-Newtonian mixing system. Subsequently, an application of the adopted optimisation framework to a non-Newtonian mixing system is shown. Additional validation of the solver in non-Newtonian Poiseuille flow and Newtonian mixing is provided in Sections 4.1 and 4.2 of Boston (2025).

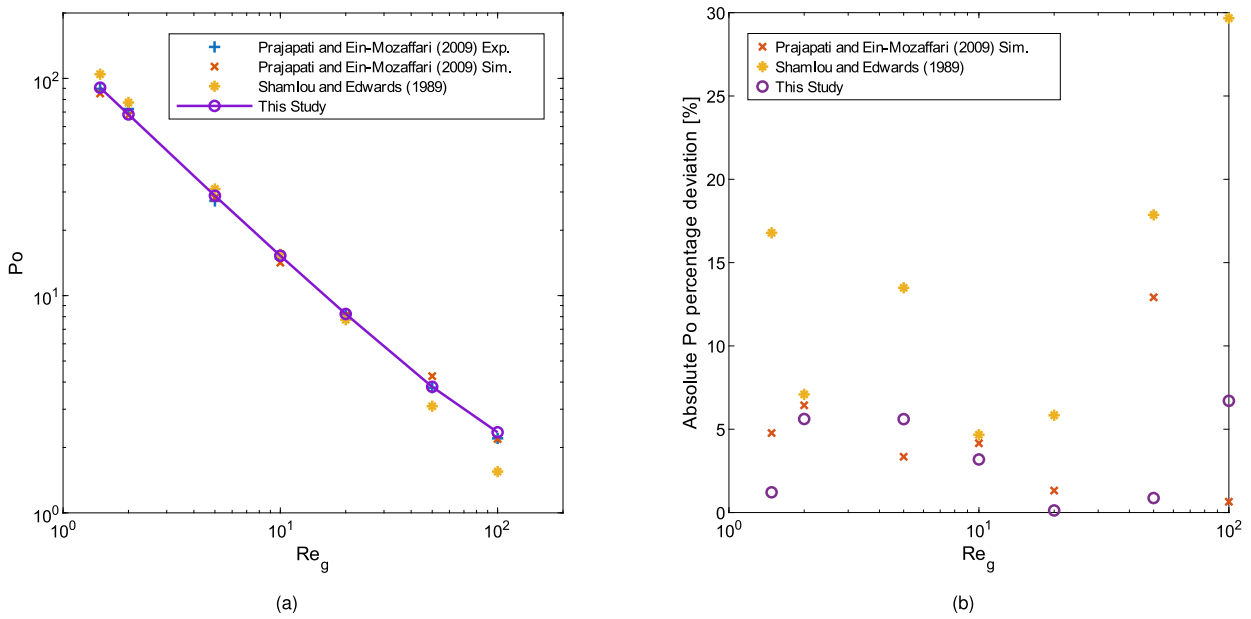

Fig. 2. (a) Po vs. $\mathrm{Re_g}$ for the impeller of Prajapati and Ein-Mozaffari (2009), with a xanthan gum solution concentration of 0.5% solids by mass. Simulation results of $\mathrm{Po}(T)$ compared against experimental and simulation results of Prajapati and Ein-Mozaffari (2009), and anchor impeller Po design equation of Shamlou and Edwards (1989). (b) Absolute percentage deviation between results and experimental results of Prajapati and Ein-Mozaffari (2009).

3.1. Validation of models - non-Newtonian mixing

The accuracy of the surrogate models rely largely on the accuracy of the hydrodynamic mixing tank model from which training data is generated. To validate the application of non-Newtonian rheology to the hydrodynamic mixing tank model, the experimental system of Prajapati and Ein-Mozaffari (2009) is modelled and their relation between Po and $\mathrm{Re_g}$ is reproduced. An anchor impeller stirs a xanthan gum solution, modelled as a Herschel–Bulkley fluid, within a cylindrical tank. The fluid simulated has the following properties: solids concentration = 0.5% by mass, $\rho = 997.36\ \mathrm{kg\ m^{-3}}$, $n = 0.11$, $k = 3\ \mathrm{Pa\ s^n}$, $\mu_0 = 13.30\ \mathrm{Pa\ s}$, $\tau_y = 1.789\ \mathrm{Pa}$, $\dot{\gamma}_c = 0.1345\ \mathrm{s^{-1}}$.

For seven different values of $\mathrm{Re_g}$ between 1.48 to 100, the deviation between simulated $\mathrm{Po}(T)$ from the experimental results of Prajapati and Ein-Mozaffari (2009) lie between 0.13% to 6.3%, showing good agreement as seen in Fig. 2. This is achieved at a grid resolution of $d_{\mathrm{imp}} = 160\,\Delta x$. Further grid refinements give little improvement at a vast computational cost; thus, an optimal grid resolution of $d_{\mathrm{imp}} = 160\,\Delta x$ to $180\,\Delta x$ is determined. Power number determined by viscous dissipation is consistently 2% to 6% lower than that determined by impeller torque, indicating a slight energy balance discrepancy, apparently independent of grid resolution. A time-averaging sampling frequency of one in every 100 time steps is seen to change time-averaged results by less than 0.5%, while ensuring less computational operations over the course of an entire simulation.

Also plotted is the experimentally-derived design equation of Shamlou and Edwards (1989) for an anchor impeller. This relation is derived in a similar manner to that of Rieger et al. (1988), which is used to estimate the Po of a helical ribbon impeller in the design procedure outlined by Grenville and Nienow (2003), as described lated in Section 3.2.5. It can be seen from Fig. 2(b) that it has a consistently higher deviation from the experimental results compared to both sets of simulation results.

Full details of system parameters and results are given in Section 4.3 of Boston (2025), and additional validation studies are provided in Chapter 4 of Boston (2025).

3.1.1. Mesh dependence analysis

A mesh dependence analysis is conducted at $\mathrm{Re_g} = 1.48$, 20.5 and 100 at six different resolutions denoted by the impeller diameter $d_{\mathrm{imp}} = 120\,\Delta x$, $160\,\Delta x$, $180\,\Delta x$, $200\,\Delta x$, $240\,\Delta x$ and $360\,\Delta x$. The system simulated is that of Prajapati and Ein-Mozaffari (2009) as per Section 3.1. The results are illustrated in Fig. 3 (see Table 4.9 of Boston (2025) for exact values).

Fig. 3(a) shows the trends of $\mathrm{Po}(T)$ against d_{imp} at each $\mathrm{Re_g}$. Fig. 3(b) compares the percentage deviation between $\mathrm{Po}(T)$ and the experimental results of literature. Here it is observed that, for $\mathrm{Re_g}$ of 1.48 and 20.5, $\mathrm{Po}(T)$ decreases past that of the literature values with increasing resolution. While the rate of change of $\mathrm{Po}(T)$ with respect to resolution appears to decrease with increasing resolution indicating convergence, this is not seen at $\mathrm{Re_g} = 1.48$. Regardless, a deviation of <10% from literature is seen. Overall, a d_{imp} of $160\,\Delta x$ to $180\,\Delta x$ appears to be a reasonable compromise between maintaining a domain sufficiently small to maintain a reasonable computational speed, while still maintaining a reasonable level of spatial resolution. Only $\mathrm{Po}(T)$ is used henceforth, and is now referred to as Po.

3.2. Optimisation of mixing conditions and impeller power consumption

An optimisation study is carried out to illustrate the framework described in Section 2.2. The system modelled is a helical ribbon impeller (HRI), as per Fig. 4, mixing a viscous, shear-thinning, power-law fluid in a cylindrical tank, with rheology described by Eqs. (3)–(4). As a reasonable compromise between computational efficiency (keeping in mind the large number of simulations to be performed) and sufficient spatial resolution, $d_{\mathrm{imp}} = 160\,\Delta x$ is chosen as justified by the mesh dependency analysis in Section 3.1.1. To ensure a low enough Ma to avoid compressibility errors, $N = 1/7200\,\mathrm{rev}\ \Delta t^{-1}$. As in previous simulations, $\rho = 8\,\mathrm{M}\ \Delta x^{-3}$. The Metzner–Otto correlation of Shamlou and Edwards (1985), Eq. (25), is used for K_S. As laminar flow is to be modelled, $\mathrm{Re_g} = 50$ as a sensible value to use for an HRI (Paul et al., 2003), and is kept constant between simulations by calculating k via Eq. (20). Viscosity boundaries for truncating the power-law are determined by the stability of the LBM solver, found to be $10^{-5}\,\Delta x^2\ \Delta t^{-1} \leq \nu \leq 100\,\Delta x^2\ \Delta t^{-1}$. This encompasses the viscosity range of real shear-thinning fluids, which have a smaller range (Landry et al., 2004).

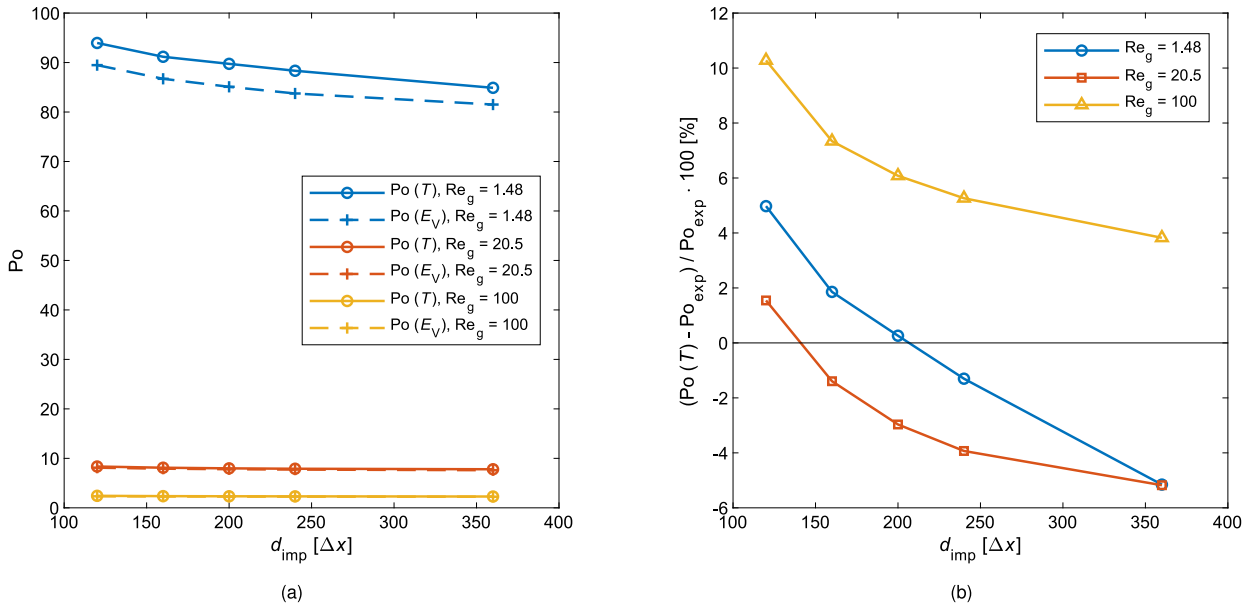

Fig. 3. Mesh dependence analysis using impeller of Prajapati and Ein-Mozaffari (2009) at Re_g of 1.48, 20.5 and 100. Mesh resolution is given in terms of impeller diameter d_{imp}, in units of lattice length. (a) Po (T) and Po (E_V) vs. d_{imp}. (b) Percentage deviation between Po (T) of simulations and Po of experiments of Prajapati and Ein-Mozaffari (2009) vs. d_{imp}.

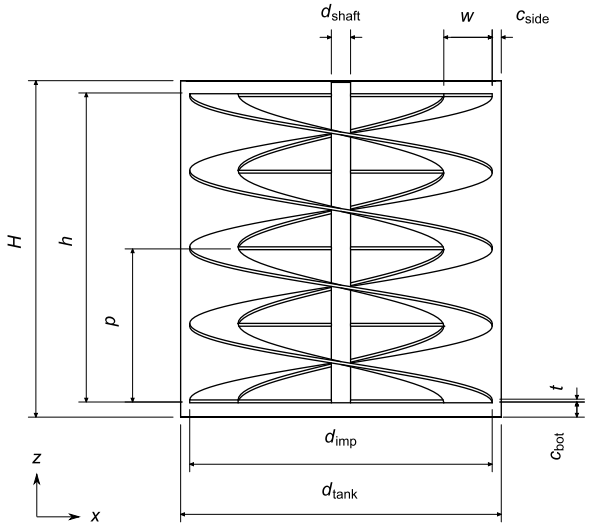

Fig. 4. Helical ribbon impeller labelled with key dimensions. xz view. Labelled quantities are as follows: tank height, H; impeller height, h; helix pitch, p; tank diameter, d_{tank}; impeller diameter, d_{imp}; shaft diameter, d_{shaft}; bottom impeller clearance, c_{bot}; side impeller clearance, c_{side}; blade width, w; blade and support rod thickness, t.

Input parameters of interest are the number of blades n_b, number of blade turns n_t (i.e. the number of times the blade revolves around the shaft along the impeller height h), blade width w, tank height H, side clearance c_{side}, top and bottom clearance c_{bot}, and flow behaviour index n. Impeller dimensions w, H, c_{side} and c_{bot} are non-dimensionalised through dividing by impeller diameter d_{imp}. Output responses measured are Po (T) (now just referred to as Po), ϕ_{dead}, and shear rate statistics (maximum $\dot{\gamma}_{max}$, volume-averaged $\dot{\gamma}_{avg}$, and standard deviation $\dot{\gamma}_{SD}$) within the fluid.

3.2.1. Screening of input parameters

To adequately search the parameter space for the impact of input parameters on output responses, a definitive screening design (Jones and Nachtsheim, 2013) is employed via *Minitab® (20.3)* (Minitab, LLC., 2021). This results in eighteen simulations, with Table 1 listing the input parameters being altered, their designated label, and their values for each state. A screening design table is provided in Section 1 of the supplementary material, detailing the states of each input for each simulation. Parameter values correspond with recommended values in literature (Delaplace et al., 2000a; Tsui and Hu, 2011; Hemrajani and Tatterson, 2003; Grenville and Nienow, 2003; Brito-De La Fuente et al., 1997; Patterson et al., 1979; Robinson and Cleary, 2012).

Table 1
Screening input parameter list and values.

Parameter	Label	–	0	+
n_b	A	One blade	N/A	Two blades
n_t	B	1.5	2.5	3.5
w	C	0.15 · d_{imp}	0.225 · d_{imp}	0.3 · d_{imp}
H	D	1.0 · d_{tank}	1.5 · d_{tank}	2.0 · d_{tank}
c_{side}	E	0.02 · d_{imp}	0.03 · d_{imp}	0.04 · d_{imp}
c_{bot}	F	0.03 · d_{imp}	0.05 · d_{imp}	0.07 · d_{imp}
n	G	0.1	0.5	0.9

A Pareto chart is created for each output response following the procedure in Section 2.2.1, with that for Po shown in Fig. 5. Plots for the other five output responses are provided in Section 2 of the supplementary material. These bar plots present the standardised effect of each input term in the model for a given output. The threshold effect is also shown as a vertical line corresponding to a p-value of 0.05. Any terms whose contributions exceed the threshold effect are included in the models. Moreover, if for a variable only the interaction term meets the threshold criterion, then the linear term is also included, e.g., the term G (n) is included in Fig. 5 because the interaction term AG $(n_b \cdot n)$ and BG $(n_t \cdot n)$ meet the threshold criterion, despite G (n) not.

It is found that the inputs with the most influential effects across all output responses are the number of blades, number of blade turns, blade width, tank height, and flow behaviour index, so these inputs are examined in the following stages, while side and bottom clearances are not. A discussion of the Pareto chart of Fig. 5, and of the others found in Figure 1 from Section 2 of the supplementary material, follows.

On power consumption, Fig. 5 shows D (H) and A (n_b) have the greatest effect. Increasing D (H) will increase tank volume, thus increasing the fluid energy lost due to viscous dissipation as per Eq. (31).

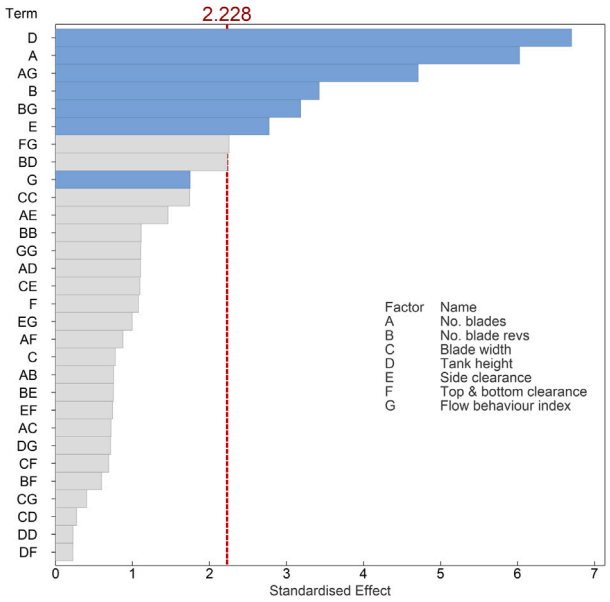

Fig. 5. Pareto chart of screening process for Po. Blue bars represent term included in regression model, grey bars represent terms omitted from regression model. Vertical red line indicates cut-off value α, below which terms are deemed to have insignificant effect on output responses. Only the thirty most significant terms are included. (For interpretation of the references to colour in this figure legend, the reader is referred to the web version of this article.)

Changing the number of blades will have a huge effect on drag felt by the blade, thus changing power consumption. B (n_t) is also a significant contributor as blade pitch will change the drag and proportion of axial flow to tangential flow. The interaction term BD ($n_t \cdot H$) can also be seen as representative of blade pitch, and is very close to the threshold (Tsui and Hu, 2011).

The Pareto chart of ϕ_{dead} shows that mixing quality, which ϕ_{dead} is a measure of, is shown to be most influenced by A (n_b) as this has a huge impact on the impeller surface area available for imparting momentum to the fluid. The presence of the interaction term BC ($n_t \cdot w$) implies that, as blade pitch changes, the impact that blade width has on mixing quality changes, presumably as the pitch will determine the flow pattern around the blade. Similarly, the presence of AC ($n_b \cdot w$) implies that the number of blades present influences the magnitude of the effect that C (w) has on ϕ_{dead}. It seems intuitive that altering blade width will have more of an impact on flow behaviour when only one blade is present. Since G (n) affects viscosity and thus momentum transfer and the fluid velocity field, it is to be expected that this is also a significant contributor to ϕ_{dead}.

Since a shear-thinning fluid is modelled, decreases in G (n) will decrease viscosity in areas of high shear and vice versa, thus having an impact on momentum transfer inside and between these areas, changing velocity gradients in a nonlinear manner, therefore impacting shear rates. It is to be expected that G (n) will have a significant impact on shear rate, and will interact with other terms that significantly affect shear rate. This is reflected in the shear rate Pareto charts, with G (n) being among the top two most significant input parameters, and having the only significant squared term. Inputs A (n_b) and G (n) have the most impact on $\dot{\gamma}_{max}$ and $\dot{\gamma}_{SD}$. Input G (n) has the highest impact on $\dot{\gamma}_{avg}$, but unexpectedly A (n_b), while still highly ranked, does not have a significant contribution to $\dot{\gamma}_{avg}$ when compared to other parameters. B (n_t) will both change surface area available and change pitch, and decreasing E (c_{side}) increases the velocity gradient in the areas of highest shear, all of which will impact $\dot{\gamma}_{avg}$.

While term E (c_{side}) is deemed a significant contributor to Po, ϕ_{dead}, $\dot{\gamma}_{avg}$, and $\dot{\gamma}_{SD}$, it is not present in any significant interaction or squared terms, suggesting a linear relationship with each output response. It is the least significant among the significant first order terms in each of these outputs, except from $\dot{\gamma}_{avg}$. It is excluded from further study, and the low value of its range is used.

F (c_{bot}) is a significant contributor to ϕ_{dead}, presumably because decreasing it reduces stagnation in the bottom and top tank clearances. It is not present in any significant squared or interaction terms, and has no significant effect on any other responses as other input parameters dominate. Therefore, it is excluded in further optimisation studies with its lower value used.

Table 2
Latin hypercube sampling input parameter ranges.

	B	C	D	G
	n_t	w/d_{imp}	H/d_{imp}	n
Min.	0.5	0.15	1.0	0.1
Max.	3.5	0.30	2.0	0.9

3.2.2. Training of regression models

After influential input parameters are determined through a screening analysis, a further series of simulations generate data to train regression equations to be used as surrogate models in place of mixing tank simulations. The input space is initially populated via Latin Hypercube Sampling (LHS) (McKay et al., 1979) for inputs B (n_t), C (w/d_{imp}), D (H/d_{imp}), and G (n), with the resulting values of n_t rounded to the closest 0.5 of an impeller turn. An initial batch of twenty simulations are run. The ranges for these values are given in Table 2. These values are used for simulations with both one blade and for two blades.

An initial batch of twenty simulations are run. The regression equations these produce are found to not be of sufficient accuracy after validation shows a roughly 30% deviation from simulation results, so an additional forty simulations are run, again using LHS, for a total of sixty simulations of training data. The complete set of training data inputs and outputs are provided in Section 3 of the supplementary material.

Training data is input to *Minitab® (20.3)* (Minitab, LLC., 2021), and 2nd order polynomial surrogate models generated using stepwise forward regression, with corrected Akaike's Information Criterion (AICc) (Hurvich and Tsai, 1989) as described in Section 2.2.1. Each regression equation takes the form

$$\begin{aligned} y =& \beta_0 + \beta_b \mathrm{B} + \beta_c \mathrm{C} + \beta_d \mathrm{D} + \beta_g \mathrm{G} \\ &+ \beta_{bb}\mathrm{B}^2 + \beta_{cc}\mathrm{C}^2 + \beta_{dd}\mathrm{D}^2 + \beta_{gg}\mathrm{G}^2 \\ &+ \beta_{bc}\mathrm{BC} + \beta_{bd}\mathrm{BD} + \beta_{bg}\mathrm{BG} + \beta_{cd}\mathrm{CD} + \beta_{cg}\mathrm{CG} + \beta_{dg}\mathrm{DG} \end{aligned} \tag{38}$$

for output response y. The coefficients of the surrogate models β are displayed in Tables 3–5. There is a choice of two coefficients for each of the 1st order terms in Table 3, corresponding to whether the impeller has one blade or two blades. Where the two coefficients are different, an interaction effect is implied between the number of impeller blades and the corresponding input parameter upon the relevant output response value. Note that shear rate statistics are calculated in lattice units. These are converted to SI units using the conversion factor C_t from Eq. (13) to obtain the relation

$$\dot{\gamma}_{SI} = \dot{\gamma}_{lu} \cdot \frac{1}{C_t} = \dot{\gamma}_{lu} \cdot \frac{N_{SI}}{N_{lu}}, \tag{39}$$

with $N_{lu} = 1/7200\,\mathrm{rev}\ \Delta t^{-1}$.

Little can be gleaned from analysing the absolute values of the coefficients since these are not normalised, however some insight can be gained by observing which terms are present. It is seen that every linear term in Table 3 makes a contribution to every output response. The β_{bb} (n_t^2) term is present for all variables, β_{cc} ($(w/d_{imp})^2$) is only present for $\dot{\gamma}_{max}$, β_{dd} $(H/d_{imp})^2$ is present in equations for Po, $\dot{\gamma}_{avg}$ and $\dot{\gamma}_{SD}$, and β_{gg} (n^2) is present in Po, ϕ_{dead} and $\dot{\gamma}_{SD}$.

Table 3
First order regression model coefficients for Eq. (38).

Output	n_b	β_0 Constant	β_b n_t	β_c w/d_{imp}	β_d H/d_{imp}	β_g n
Po [–]	1	3.610	0.3880	−3.910	0.3500	−4.001
	2	4.170	0.8610	−12.56	1.860	−0.7780
ϕ_{dead} [%]	1	17.55 %	−1.951 %	−32.86 %	−1.359 %	−9.000 %
	2	9.430 %	−1.575 %	−16.98 %	−1.359 %	−6.460 %
$\dot{\gamma}_{max}$ [Δt^{-1}]	1	0.103 41 Δt^{-1}	−0.020 32 Δt^{-1}	−0.2047 Δt^{-1}	0.025 14 Δt^{-1}	−0.065 37 Δt^{-1}
	2	0.091 53 Δt^{-1}	−0.017 80 Δt^{-1}	−0.2047 Δt^{-1}	0.020 08 Δt^{-1}	−0.050 65 Δt^{-1}
$\dot{\gamma}_{avg}$ [Δt^{-1}]	1	0.001 454 Δt^{-1}	$2.220 \cdot 10^{-4}$ Δt^{-1}	$6.590 \cdot 10^{-4}$ Δt^{-1}	$-7.890 \cdot 10^{-4}$ Δt^{-1}	$3.880 \cdot 10^{-4}$ Δt^{-1}
	2	0.002 194 Δt^{-1}	$1.810 \cdot 10^{-4}$ Δt^{-1}	−0.001 075 Δt^{-1}	$-7.890 \cdot 10^{-4}$ Δt^{-1}	$5.300 \cdot 10^{-4}$ Δt^{-1}
$\dot{\gamma}_{SD}$ [Δt^{-1}]	1	0.003 188 Δt^{-1}	$2.390 \cdot 10^{-4}$ Δt^{-1}	$-6.820 \cdot 10^{-4}$ Δt^{-1}	$-9.660 \cdot 10^{-4}$ Δt^{-1}	−0.002 449 Δt^{-1}
	2	0.003 481 Δt^{-1}	$4.530 \cdot 10^{-4}$ Δt^{-1}	$6.490 \cdot 10^{-4}$ Δt^{-1}	−0.001 221 Δt^{-1}	−0.002 624 Δt^{-1}

Table 4
Second order squared regression model coefficients for Eq. (38).

Output	β_{bb} n_t^2	β_{cc} $(w/d_{imp})^2$	β_{dd} $(H/d_{imp})^2$	β_{gg} n^2
Po [–]	0.3188	0	1.061	3.663
ϕ_{dead} [%]	−0.1149 %	0 %	0 %	3.407 %
$\dot{\gamma}_{max}$ [Δt^{-1}]	0.001 639 Δt^{-1}	0.4010 Δt^{-1}	0 Δt^{-1}	0 Δt^{-1}
$\dot{\gamma}_{avg}$ [Δt^{-1}]	$2.000 \cdot 10^{-5}$ Δt^{-1}	0 Δt^{-1}	$1.970 \cdot 10^{-4}$ Δt^{-1}	0 Δt^{-1}
$\dot{\gamma}_{SD}$ [Δt^{-1}]	$6.200 \cdot 10^{-5}$ Δt^{-1}	0 Δt^{-1}	$4.210 \cdot 10^{-4}$ Δt^{-1}	0.001 441 Δt^{-1}

Table 5
Second order interaction regression model coefficients for Eq. (38).

Output	β_{bc} $n_t \cdot (w/d_{imp})$	β_{bd} $n_t \cdot (H/d_{imp})$	β_{bg} $n_t \cdot n$	β_{cd} $(w/d_{imp}) \cdot (H/d_{imp})$	β_{cg} $w \cdot n$	β_{dg} $(H/d_{imp}) \cdot n$
Po [–]	−4.144	−0.7346	1.905	16.40	0	−3.273
ϕ_{dead} [%]	4.270 %	0.6330 %	0 %	0 %	11.40 %	0 %
$\dot{\gamma}_{max}$ [Δt^{-1}]	0.018 31 Δt^{-1}	−0.001 639 Δt^{-1}	0.009 650 Δt^{-1}	−0.040 30 Δt^{-1}	0.074 80 Δt^{-1}	−0.006 090 Δt^{-1}
$\dot{\gamma}_{avg}$ [Δt^{-1}]	$-4.650 \cdot 10^{-4}$ Δt^{-1}	$-9.900 \cdot 10^{-5}$ Δt^{-1}	0 Δt^{-1}	0.001 662 Δt^{-1}	0 Δt^{-1}	$-1.320 \cdot 10^{-4}$ Δt^{-1}
$\dot{\gamma}_{SD}$ [Δt^{-1}]	0 Δt^{-1}	$-2.770 \cdot 10^{-4}$ Δt^{-1}	$1.190 \cdot 10^{-4}$ Δt^{-1}	0 Δt^{-1}	0 Δt^{-1}	0 Δt^{-1}

Interaction effects between A (n_b) and the first order terms on the output responses can be analysed by examining the relative differences in coefficient values between the equations for one blade and two blades in Table 3. For example, the value of β_c (w/d_{imp}) is over 3 times that for two blades than for one blade for Po, indicating C (w/d_{imp}) has a greater relative contribution to Po when one blade is present. With two blades, increasing the blade width will increase the blade surface area and thus impeller drag by a greater amount than with one blade. By contrast, when looking at ϕ_{dead}, its value for one blade is roughly double that of two blades in line with reasoning in Section 3.2.1. Similar trends are seen for B (n_t) and D (H/d_{imp}), although the coefficients for D (H/d_{imp}) on ϕ_{dead} are the same, indicating no interaction between A (n_t) and D (H/d_{imp}). The value of β_g (n) is over 5 times less for two blades than for one blade for Po, which as shown in Fig. 5, can be attributed to increasing the number of blades having a far larger effect on power consumption than changing the flow behaviour index.

3.2.3. Surrogate model validation

Next, the regression models must be validated against simulation data separate to that upon which they were trained. An additional four simulations are run for this purpose. Their input parameters are shown in Table 6, with results provided in Section 4 of the supplementary material. The percentage deviations between the surrogate model results and simulation results are calculated as

$$\%\, deviation = \frac{Surrogate - Simulation}{Simulation} \cdot 100 \tag{40}$$

and plotted against n in Fig. 6.

A relatively high deviation is present at the lowest value of n for all outputs except standard deviation of shear rate, but all values lie below a deviation of 20%. For shear rate statistics, the deviation is consistently below 11%, as is Po for the highest three values of n. Error for ϕ_{dead} lies between 9.7% to 18%. To further reduce this error, the surrogate models should be trained on additional simulations. An interesting avenue of research would be comparing the accuracy of surrogate models trained on a gradually increasing volume of simulations. The relatively low error values of $\dot{\gamma}$ statistics may indicate a lack of sensitivity with respect to the input parameters.

Table 6
Surrogate model validation input parameters.

n	n_b	n_t	w	H
0.2	2	3.5	$0.1575 \cdot d_{imp}$	$1.05 \cdot d_{tank}$
0.4	2	3	$0.1575 \cdot d_{imp}$	$1.05 \cdot d_{tank}$
0.6	1	3.5	$0.2925 \cdot d_{imp}$	$1.05 \cdot d_{tank}$
0.8	1	2.5	$0.2925 \cdot d_{imp}$	$1.05 \cdot d_{tank}$

3.2.4. Minimisation of output responses

Now equipped with surrogate models for each output, the Composite Desirability Function (CDF) (Derringer and Suich, 1980) discussed in Section 2.3, that utilises the surrogate models, is maximised using the proprietary Reduced Gradient Algorithm (RGA) of *Minitab® (20.3)* (Minitab, LLC., 2021) to provide solutions for the multi-objective optimisation problem of minimising Po (T), ϕ_{dead}, and $\dot{\gamma}_{max}$.

Five solutions to five different minimisation problems are generated: to compare the recommended configurations for different flow behaviour indices: for the first problem, n is allowed to vary, and for the other four, n is held constant at 0.2, 0.4, 0.6 and 0.8. The purpose of this is to compare the recommendations given for a range of different fluids, with n typically being inversely proportional to solids concentration in shear-thinning fluids (Landry et al., 2004). An importance w_i of 2 is

Table 7
Optimisation results.

Problem	n	Composite desirability	Po (T)	ϕ_{dead}	$\dot{\gamma}_{max}$	A n_b	B n_t	C w	D H	G n
1	–	0.94	5.806	3.919 %	0.040 76 Δt^{-1}	1	1.17	$0.2963 \cdot d_{imp}$	$1.025 \cdot d_{tank}$	0.88
2	0.2	0.83	6.696	4.432 %	0.053 40 Δt^{-1}	1	2.80	$0.2963 \cdot d_{imp}$	$1.025 \cdot d_{tank}$	0.2
3	0.4	0.87	6.221	4.135 %	0.052 17 Δt^{-1}	1	2.11	$0.2963 \cdot d_{imp}$	$1.025 \cdot d_{tank}$	0.4
4	0.6	0.91	5.820	4.018 %	0.049 59 Δt^{-1}	1	1.44	$0.2948 \cdot d_{imp}$	$1.025 \cdot d_{tank}$	0.6
5	0.8	0.93	5.811	3.873 %	0.043 23 Δt^{-1}	1	1.29	$0.2963 \cdot d_{imp}$	$1.025 \cdot d_{tank}$	0.8

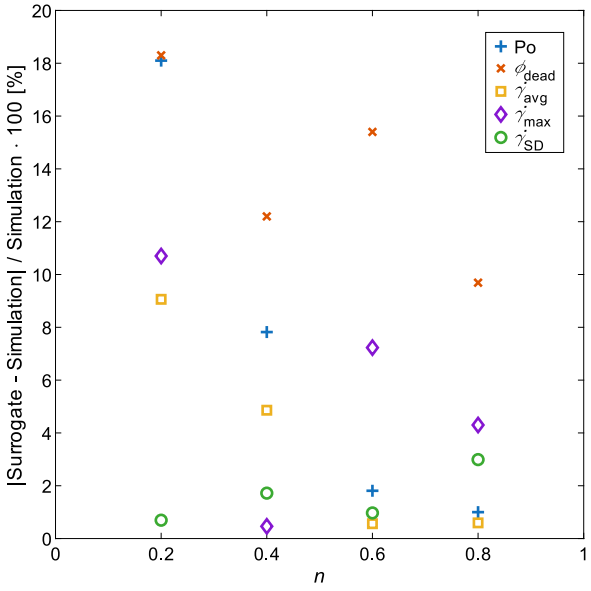

Fig. 6. Results of surrogate model validation, plotting percentage deviation of surrogate model results from simulation results against flow behaviour index n, for output responses of power number Po, percentage of dead volume ϕ_{dead}, shear rate average $\dot{\gamma}_{avg}$, shear rate maximum $\dot{\gamma}_{max}$, and shear rate standard deviation $\dot{\gamma}_{SD}$.

assigned to Po, 0.5 to ϕ_{dead}, and 0.5 to $\dot{\gamma}_{max}$. These values are chosen somewhat arbitrarily, but on the assumption that Po minimisation is more important than minimisation of ϕ_{dead} and $\dot{\gamma}_{max}$. The top solution for each optimisation is shown in Table 7. This is accompanied by the value of composite desirability for each solution, which is a measure of how well the competing objectives have been collectively met, with a value of 1 meaning each objective is perfectly minimised.

It can be seen that the optimised Po ranges from 5.806 to 6.696 for various values of n. There is a trend of decreasing Po with the increase in n as the larger value of n will result in lower apparent viscosity of the fluid regions of low shear, which make up more of the volume than the areas of high shear adjacent to the impeller. The same trend is found for the other two objectives, ϕ_{dead} and $\dot{\gamma}_{max}$, with respect to n. Momentum transfer within the fluid will be improved in regions of low shear, if these regions have a lower apparent viscosity.

In terms of the decision variables, the number of blade turns (B) is found to be most sensitive to the various values of n. The optimisation suggests a lower number of turns as n increases, resulting in a lower apparent viscosity as reasoned above. For a more viscous fluid, if the number of turns of the blade is decreased, there will be less contact area available for the impeller to impart mixing energy to the fluid, and pitch will be increased thus decreasing drag.

Across all values of n, it is recommended to use one impeller blade rather than two, which will drastically reduce the power consumption, while increasing the percentage of dead volume. This seems to be compensated for by maximising the blade width (C), which will increase drag and the amount of momentum transferred to the fluid, thus increasing Po and decreasing ϕ_{dead}. Also for all values of n, the tank height (D) is minimised.

Table 8
Optimisation method validation input parameters.

Design no. [–]	Weightings Po [–]	Weightings ϕ_{dead} [–]	Input parameters n [–]	n_b [–]	n_t [–]	w [m/d_{imp}]	H [m/d_{tank}]
1	–	–	0.367	2	1	0.16	1.05
2	1	1	0.367	2	0.5	0.2228	1.05
3	10	0.1	0.367	1	1.5	0.2400	1.05
4	0.1	10	0.367	2	3.5	0.2963	1.05

3.2.5. Optimisation method validation

To assess the accuracy of the surrogate models developed in the previous section, and their ability to produce an optimised mixing system in a practical application, additional mixing systems are designed and compared against the mixing tank design methodology outlined in Grenville and Nienow (2003) for laminar blending using empirical design equations. This serves as a proof-of-concept for the design of a mixing tank to stir a high-solids concentration (>10% by mass) liquid.

First, the design equations presented by Grenville and Nienow (2003) are used to design a mixing tank system. Then, the surrogate models developed in Section 3.2.2 are used to design three "optimised" alternatives. The input parameters that minimise the objectives the best, according to the highest value of the CDF of these optimisations are shown in Table 8. Simulations of each of the four designs using these input parameters are run, and for each, power number is calculated using the design equation of Rieger et al. (1988), and from the surrogate model of Eq. (38) and Tables 3–5. These designs are then compared, using the simulation results as a baseline as justified in Section 3.1. In this comparison, the constraints of the design variables are kept the same as the ones used in the regression model development. One important difference between this design and the methodology outlined in Grenville and Nienow (2003) is fixing the generalised Reynolds number Re_g at 50 since the regression model is developed for this Re_g. Mixing of a shear thinning fluid is considered in a tank with helical ribbon impeller and tank diameter of approximately $d_{tank} = 2$ m. The flow behaviour index for the fluid is taken as $n = 0.367$, and flow consistency $k = 5.885$ Pa s^n, which corresponds to a 12.1% solids manure slurry (Dapelo et al., 2019; Landry et al., 2004).

Four mixing tank designs are produced. Design 1 is created using the methodology of Grenville and Nienow (2003). Designs 2, 3 and 4 are produced using the optimisation framework proposed in the previous sections, with different weightings of Po and ϕ_{dead}.

Following the design methodology in Grenville and Nienow (2003), the suggested impeller diameter falls in the range $0.90 \cdot d_{tank} \leq d_{imp} \leq 0.95 \cdot d_{tank}$; $c_{side} = 0.03 \cdot d_{imp}$ is chosen as per the surrogate model range, therefore $d_{imp} = 0.9434 \cdot d_{tank}$ is assumed. Impeller rotational frequency N is found by solving Eq. (20) with a standard value of $K_S = 30$ (Grenville and Nienow, 2003). This is then converted from rev s^{-1} to rpm and the closest value from Table 6.2 of standard impeller speeds in Hemrajani and Tatterson (2003) is used as the value for N (repeated as Table 5.10 in Boston (2025)). A final value for d_{imp} is calculated from Eq. (20), and d_{tank} is found as

$$d_{tank} = 2c_{side} + d_{imp}\,. \tag{41}$$

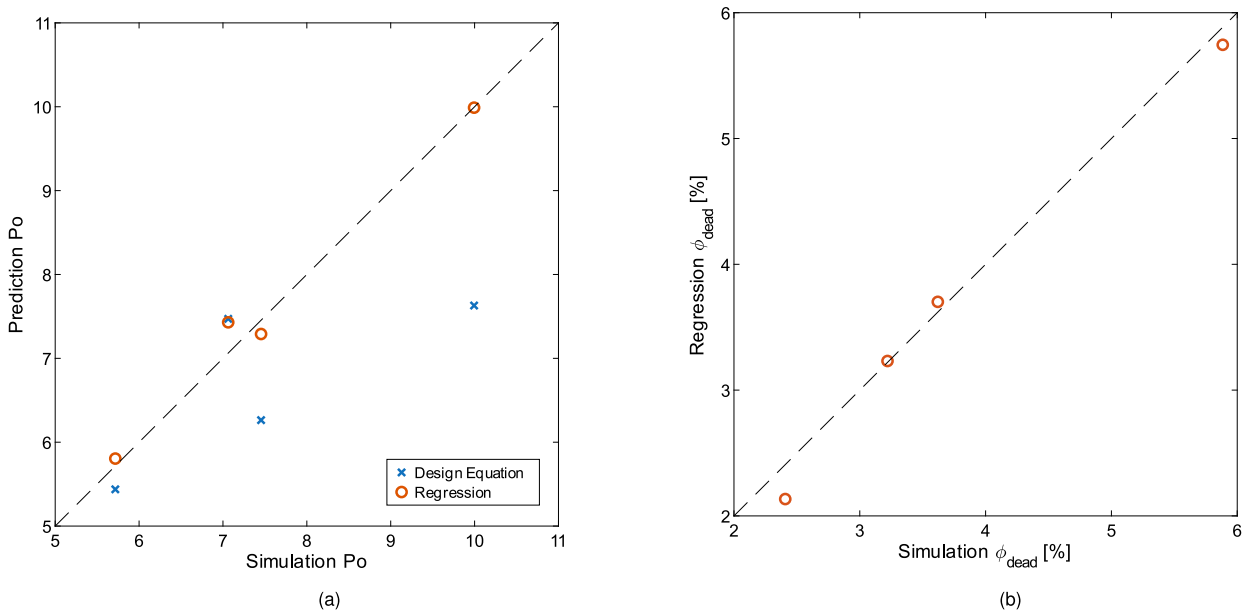

Fig. 7. (a) Comparison of the power number Po obtained from design equation based design (Grenville and Nienow, 2003) and the designs using the surrogate model developed in this work. The reference Po is obtained from the LBM simulation of the process. (b) Comparison of the dead volume fraction ϕ_{dead} for the surrogate model with the reference value obtained from LBM simulation.

The number of impeller blades is assumed to be $n_b = 2$, and tank height $H = 1.05 \cdot d_{tank}$. Pitch and blade height are $p = h = d_{imp}$. While it is assumed in Grenville and Nienow (2003) that blade width $w = 0.10 \cdot d_{imp}$, this lies outwith the training data, so it is decided that $w = 0.16 \cdot d_{imp}$.

The power number Po and Re_g are related by the impeller geometric constant K_P (dimensionless) as per

$$Po = \frac{K_P}{Re_g}, \tag{42}$$

with K_P calculated as per Rieger et al. (1988), i.e.

$$K_P = 82.8 \left(\frac{h}{d_{imp}}\right) \left(\frac{c_{side}}{d_{imp}}\right)^{-0.38} \left(\frac{p}{d_{imp}}\right)^{-0.35} \left(\frac{w}{d_{imp}}\right)^{0.20} n_b^{0.78}. \tag{43}$$

In addition to calculating Po, K_P allows checking that the blend time θ is below a target value of around 10 min as per (Grenville and Nienow, 2003) —

$$N\theta = 896 \cdot 10^3 K_P^{-1.69}. \tag{44}$$

Eq. (27) is used to find P. This can be converted from W to hp and matched with a standard motor speed (Hemrajani and Tatterson, 2003).

In summary, the decision variables for the optimised design obtained using the design equations (Grenville and Nienow, 2003) and the methodology proposed in this work are presented in Table 9.

When using empirical values for minimum and maximum dynamic viscosities μ_{min} and μ_{max}, these must be converted from SI to lattice units. This can be achieved using either the conversion factors from Eqs. (11) and (13), or using the Reynolds number. For using conversion factors,

$$\mu_{lu} = \mu_{SI} \cdot \frac{C_l C_t}{C_m}. \tag{45}$$

For using Re

$$Re = \frac{\rho_{SI} N_{SI} d_{imp,SI}^2}{\mu_{SI}}, \tag{46}$$

$$\mu_{lu} = \frac{\rho_{lu} N_{lu} d_{imp,lu}^2}{Re}. \tag{47}$$

Both methods give the same value of μ. Since the values of μ_{min} and μ_{max} used in the training data are determined by the stability of the LBM as opposed to being based on empirical data, these same values are used in this base case. To find $\dot{\gamma}_{min}$ and $\dot{\gamma}_{max}$, μ_{max} and μ_{min} are substituted respectively for η in Eq. (3).

Table 9
Optimisation method validation system geometry, fluid properties, and other system properties.

Quantity	Units	Value
d_{tank}	m	1.788
H	m	1.877
d_{imp}	m	1.686
h	m	1.686
c_{side}	m	0.051
% Solids	%	12.1
n	–	0.367
ρ	kg m^{-3}	1001.73
k	Pa s^n	5.885
N	rpm	4.0
Re_g	–	50
K_P	–	381.5
θ	s	604
K_S	–	30

The power number Po obtained from the design equation (Rieger et al., 1988) and the regression based surrogate model (developed in this work) are compared by taking the Po from LBM simulations as the reference. These results are plotted in Fig. 7(a). Ideally, the Po calculated using both approaches should match very closely with the reference value, i.e., the data points should lie on the diagonal line. However, it can be seen that the regression based model matches the reference Po closely (percentage error $\leq$ 6%) while larger error (percentage error $\leq$ 24%) is found for the design equation. The error becomes more prominent at higher Po.

In Fig. 7(b), the dead volume obtained from the regression model is plotted against the reference data obtained from LBM simulation. Note that the design equation based design cannot predict the dead volume, however it can predict the blend time. For CFD simulations to accurately implement this, advection–diffusion or particle physics must be incorporated. Also note that the blend time estimated by Eq. (44) does not account for the fluid rheology. It can be seen that very good agreement is found for the dead volume as the data points almost lie on the diagonal line.

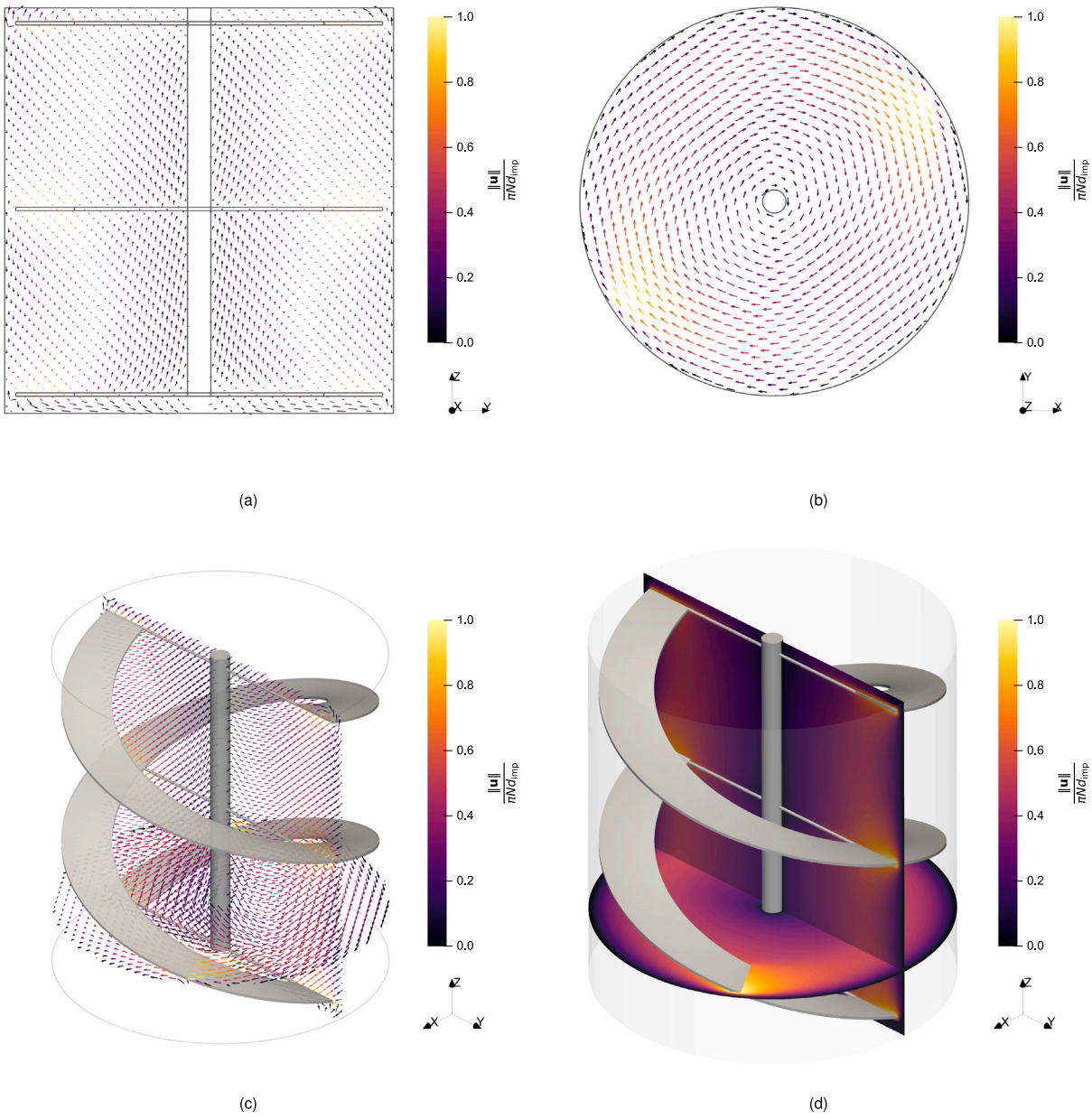

Fig. 8. Velocity vectors of design 1 after 10 impeller revolutions. Colour indicates velocity magnitude normalised by impeller tip speed. $Re_g = 50$, $n = 0.367$, $k = 5.885$ Pa s^n. (a) yz cross section at $x = d_{tank}/2$. (b) xy cross section at $z = H/5$. (c) Full 3D view of system with cross sections as in (a) and (b). (d) Velocity field only. (For interpretation of the references to colour in this figure legend, the reader is referred to the web version of this article.)

From the results in Table 10, a similarly low deviation between shear rate statistics and simulation results are seen. Therefore, the results suggest that the developed surrogate model for power number can reproduce simulation results with more precision than the design equation based model. However, since the surrogate model is trained upon the simulation data, this is to be somewhat expected , so this conclusion should be treated with caution. Also note that the design equation based model already gives close to an optimal configuration for the given design constraints, with design 1 giving a good balance between Po, ϕ_{dead}, and shear rate statistics.

Velocity vectors for the simulation of design 1 are shown in Fig. 8. The plots are coloured by velocity magnitude normalised by impeller tip speed, and are taken at 10 impeller revolutions. The areas of highest velocity occur at the impeller tip, and lowest velocity occurs adjacent to the tank walls and the impeller shaft.

In summary, the design equation based model has a wider range of applicability , so can be used when CFD simulations cannot be run due to lack of resources or time. In contrast, the proposed optimisation framework can be used when a more detailed insight into the design of the mixing tank is required and running CFD simulations is feasible.

4. Conclusions and future research

In this work, an optimisation framework based on DoE and surrogate modelling is presented in designing a mixing tank for shear-thinning liquids, with an aim to minimising three objectives — the energy consumption in mixing, the percentage of dead volume within the tank, and the maximum shear rate within the tank. Minimisation of these objectives are important in a variety of applications such as in anaerobic digestion processes to improve product yields and to maximise profits. The optimisation framework allows the identification of the most influential design parameters for the mixing tank design, and to subsequently develop surrogate models to be used in rapid

Table 10
Optimisation method validation results.

Design no. [–]	Rieger et al. (1988)	Surrogate model results					Simulation results				
	Po [–]	Po [–]	ϕ_{dead} [%]	$\dot{\gamma}_{avg}$ [s^{-1}]	$\dot{\gamma}_{max}$ [s^{-1}]	$\dot{\gamma}_{SD}$ [s^{-1}]	Po [–]	ϕ_{dead} [%]	$\dot{\gamma}_{avg}$ [s^{-1}]	$\dot{\gamma}_{max}$ [s^{-1}]	$\dot{\gamma}_{SD}$ [s^{-1}]
1	7.471	7.430	3.702	0.8910	26.59	1.088	7.063	3.620	0.8627	25.15	1.030
2	6.263	7.290	3.231	0.8964	27.42	1.035	7.454	3.220	0.9130	28.00	0.9939
3	5.438	5.805	5.745	0.7517	27.07	0.9104	5.717	5.885	0.7465	26.48	0.8899
4	7.630	9.989	2.134	0.9396	21.58	1.712	9.994	2.408	0.9301	20.37	1.670

process optimisation. The polynomial based surrogate model is able to accurately predict the objective functions instantaneously as compared to the hydrodynamic model of the mixing system based on the continuity and the conservation of momentum equations. However, the accuracy of the surrogate model cannot be guaranteed outside the range of design variables which have been used in the model development — an issue inherent in many data-based models. It has been further shown that the proposed methodology is able to predict the power number of simulations with greater accuracy than design equation based design equations. A quantitative summary of the accuracy of the methods used follows.

The surrogate models used in optimisation differ from simulation results by up to 18% for power number and percentage of dead volume within the tank, by up to 9.1% for average shear rate, 11% for maximum shear rate, and 5.5% for standard deviation of shear rate. The power number matches simulation results closer than design equation based relations do, although this is perhaps to be somewhat expected.

As in many engineering problems, optimising the mixing conditions within a mixing tank is a complex task with multiple competing objectives: as impeller power consumption and shear rate is decreased, the percentage of dead volume will necessarily increase. There is no single "correct" solution, but a range of solutions can be generated depending upon which objective is favoured. The design equation based method, leading to design 1 detailed in Tables 8 and 10, gives little scope for fine-tuning these competing variables. The values of power number in designs 2 to 4 change by as much as 43%, while the percentage of dead volume changes by 59%, and maximum shear rate changes by 27%, illustrating how the parameter space can be searched with objectives weighted according to preference. This allows a more informed decision about the design.

Meanwhile, the optimisations in Section 3.2.4, whereby the flow behaviour index is fixed at different increments, and the power number, percentage of dead volume, and maximum shear rate are minimised with a weighting in favour of minimising power number, demonstrate the use of the model in identifying trends. Here, the optimisation method minimises the number of blades and tank height, and maximises the blade width for all cases, then increases the blade pitch to an optimal value as behaviour index increases by changing the number of impeller turns about the shaft. It is seen in Table 7 that all three output responses decrease as flow behaviour index is increased.

In summary, for the first time to the best of knowledge, a systematic multi-objective optimisation is performed with a DoE RSM framework, to minimise power consumption, dead volume percentage, and maximum shear, of a mixing tank containing a non-Newtonian, shear-thinning, power-law liquid, stirred by an HRI, using the LBM to model hydrodynamics.

It would be beneficial for the surrogate models to undergo further validation to firmly determine their accuracy, and to determine their ability to extrapolate results outwith their training data range. Improvements upon this work may include utilising a machine learning based surrogate model in the optimisation framework — for example, the a surrogate model could be generated using an Artificial Neural Network (ANN), although this may require at least an order of magnitude more simulation training data as can be seen from recent studies (Wang et al., 2019; Choong et al., 2020; Li and Sansalone, 2022; Bibeau et al., 2023; Kang et al., 2024; Rahimzadeh et al., 2024; Zhao et al., 2024). The amount of required simulations may be reduced by taking a physics-informed machine learning approach (Cai et al., 2021), for example by augmenting the loss function to account for discrepancies between model predictions and the continuity and momentum equations (Choi et al., 2022). This could certainly provide an improvement to the surrogate model over an RSM approach. Moreover, other processes such as advection–diffusion, and reactions (Tobo et al., 2020), can be incorporated into the hydrodynamic model for the simulation of a wider range of industrial applications such as reactors and anaerobic digestion, and to more meaningfully predict the quality of mixing.

Nomenclature

Abbreviations

AICc	Corrected Akaike's information criterion
ANN	Artificial Neural Network
CDF	Composite desirability function
CFD	Computational fluid dynamics
DoE	Design of experiments
DSD	Definitive screening design
FEM	Finite element method
FVM	Finite volume method
HRI	Helical ribbon impeller
IBM	Immersed boundary method
LBM	Lattice Boltzmann method
LHS	Latin hypercube sampling
OVAT	One-variable-at-a-time
RGA	Reduced gradient algorithm
RSM	Response surface methodology
SPH	Smoothed-particle hydrodynamics

Greek Symbols

α	Threshold p-value	–
$\boldsymbol{\alpha}^{\pm}$	Velocity moments of distribution function	varies
β	Surrogate model term coefficient	varies
$\dot{\gamma}$	Shear rate	s^{-1}
$\dot{\gamma}_{avg}$	Average shear rate in shearing region	s^{-1}
$\dot{\gamma}_{avg}$	Average shear rate in tank fluid	s^{-1}
$\dot{\gamma}_{c}$	Critical shear rate	s^{-1}
$\dot{\gamma}_{max}$	Maximum shear rate as per rheological model	s^{-1}
$\dot{\gamma}_{max}$	Maximum shear rate in tank fluid	s^{-1}
$\dot{\gamma}_{min}$	Minimum shear rate as per rheological model	s^{-1}
$\dot{\gamma}_{SD}$	Standard deviation of shear rate in tank fluid	s^{-1}

$\boldsymbol{\epsilon}$	Strain rate tensor	s^{-1}
η	Apparent dynamic viscosity	kg m^{-1} s^{-1}
θ	Blend time	s
μ	Shear-independent dynamic viscosity	kg m^{-1} s^{-1}
μ_0	Yielding dynamic viscosity	kg m^{-1} s^{-1}
μ_{max}	Maximum dynamic viscosity as per rheological model	kg m^{-1} s^{-1}
μ_{min}	Minimum dynamic viscosity as per rheological model	kg m^{-1} s^{-1}
ν	Kinematic viscosity	m^2 s^{-1}
ν_{app}	Apparent kinematic viscosity	m^2 s^{-1}
ρ	Mass density	kg m^{-3}
τ	Shear stress	kg m^2 s^{-2}
$\boldsymbol{\tau}$	Viscous stress tensor	kg m^{-1} s^{-2}
$\boldsymbol{\tau}_{SGS}$	Subgrid-scale stress tensor	kg m^{-1} s^{-2}
τ_y	Yield shear stress	kg m^{-1} s^{-2}
ϕ_{dead}	Percentage of dead volume in tank	%

Latin Symbols

a	Number of coefficients in regression model	–
AICc	Value of corrected Akaike's information criterion	–
b	Sample size of training data for regression model	–
c_{bot}	Impeller bottom clearance	m
C_l	Length conversion factor	s Δx^{-1}
C_m	Mass conversion factor	kg M^{-1}
c_s	Speed of sound	m s^{-1}
c_{side}	Impeller side clearance	m
C_t	Time conversion factor	s Δt^{-1}
D	Composite desirability	–
d_i	Individual desirability of response i	–
d_{imp}	Impeller blade diameter	m
d_{shaft}	Impeller shaft diameter	m
d_{tank}	Tank diameter	m
E_V	Viscous dissipation energy	kg m^2 s^{-3}
$\mathbf{F}$	Specific body force	kg m^{-2} s^{-1}
$\mathbf{f}$	Distribution function	kg s^3 m^{-6}
$\mathbf{F}^{\pm}$	Fourth order distribution function moments	kg m s^{-4}
H	Tank height	m
h	Impeller blade height	m
h_{cross}	Impeller crossbar height	m
i	Response integer	–
k	Flow consistency index	kg m^{-1} s^{n-2}
K_P	Impeller geometric constant	–
K_S	Metzner–Otto shear constant	–
$\mathcal{L}$	Likelihood function	–
M	Lattice mass unit	kg
Ma	Mach number	–
N	Impeller rotational frequency	s^{-1}
n	Flow behaviour index	–
n_b	Number of impeller blades	–
n_t	Number of blade turns around shaft	–
P	Impeller power consumption	kg m^2 s^{-3}
p	Impeller blade pitch	m
p	Pressure	kg m^{-1} s^{-2}
p	Probability of failing to reject null-hypothesis	–
Po	Impeller power number	–
Re	Impeller Reynolds number	–
Re_g	Generalised impeller Reynolds number	–
r_i	Weight of response i	–
T	Impeller torque	kg m^{-1} s^{-2}
t	Impeller blade thickness	m
t	Time	s
$\mathbf{T}^{\pm}$	Third order distribution function moments	kg s^{-3}
Δt	Duration of one time step	s
$\mathbf{u}$	Fluid velocity vector	m s^{-1}
$\lvert\mathbf{u}\rvert_{max}$	Maximum fluid velocity vector magnitude	m s^{-1}
u_{tip}	Impeller tip speed	m s^{-1}
V	Tank volume	m^3
w	Impeller blade width	m
w_i	Importance of response	–
x	x-coordinate	m
$\mathbf{x}$	Coordinate vector	m
Δx	Spacing between adjacent lattice nodes	m
y	Surrogate model response value	varies
y	y-coordinate	m
$\hat{Y}_i$	Prediction of response i from surrogate model	varies
$Y_{i,max}$	Maximum acceptable response value	varies
$Y_{i,min}$	Minimum acceptable response value	varies
z	z-coordinate	m

CRediT authorship contribution statement

Liam Merrick Boston: Writing – original draft, Visualization, Methodology, Formal analysis. **Jos Derksen:** Writing – review & editing, Supervision, Software, Conceptualization. **Aniruddha Majumder:** Writing – review & editing, Supervision, Methodology.

Declaration of competing interest

The authors declare that they have no known competing financial interests or personal relationships that could have appeared to influence the work reported in this paper.

The author is an Editorial Board Member/Editor-in-Chief/Associate Editor/Guest Editor for this journal and was not involved in the editorial review or the decision to publish this article.

Acknowledgements

This study was funded by The LEVERHULME TRUST, United Kingdom (Grant DS-2017-073). Liam Merrick Boston, a Leverhulme Trust Doctoral Scholar, is part of the 15 PhD scholarships of the "Leverhulme Centre for Doctoral Training in Sustainable Production of Chemicals and Materials" at the University of Aberdeen (Scotland, United Kingdom). Also acknowledged is the Digital Research team at the University of Aberdeen for permitting the use of the Maxwell supercomputing cluster to run simulations.

Appendix A. Derivation of strain rate tensor from distribution function

The derivation of Eq. (A.5) follows. The velocity moments of the distribution function are represented by $\boldsymbol{\alpha}^{\pm}$, with $\boldsymbol{\alpha}^{-}$ pre-collision, and

$\boldsymbol{\alpha}^{+}$ post-collision (Somers, 1993; Eggels and Somers, 1995). For the D3Q18 velocity set employed here, this reads

$$\begin{aligned}\boldsymbol{\alpha}^{\pm}(\mathbf{x},t) = \Big[& \rho, \rho u_x \pm \frac{1}{2}F_x, \rho u_y \pm \frac{1}{2}F_y, \rho u_z \pm \frac{1}{2}F_z, \\ & \rho\left(u_x u_x + \tau_{\mathrm{SGS},xx}\right) + \rho\left(\frac{\pm 1 - 6\nu}{6}\right)\left(2\partial_x u_x\right), \\ & \rho\left(u_x u_y + \tau_{\mathrm{SGS},xy}\right) + \rho\left(\frac{\pm 1 - 6\nu}{6}\right)\left(\partial_x u_y + \partial_y u_x\right), \\ & \rho\left(u_y u_y + \tau_{\mathrm{SGS},yy}\right) + \rho\left(\frac{\pm 1 - 6\nu}{6}\right)\left(2\partial_y u_y\right), \\ & \rho\left(u_x u_z + \tau_{\mathrm{SGS},xz}\right) + \rho\left(\frac{\pm 1 - 6\nu}{6}\right)\left(\partial_x u_z + \partial_z u_x\right), \\ & \rho\left(u_y u_z + \tau_{\mathrm{SGS},yz}\right) + \rho\left(\frac{\pm 1 - 6\nu}{6}\right)\left(\partial_y u_z + \partial_z u_y\right), \\ & \rho\left(u_z u_z + \tau_{\mathrm{SGS},zz}\right) + \rho\left(\frac{\pm 1 - 6\nu}{6}\right)\left(2\partial_z u_z\right), \\ & T_1^{\pm}, T_2^{\pm}, T_3^{\pm}, T_4^{\pm}, T_5^{\pm}, T_6^{\pm}, F_1^{\pm}, F_2^{\pm}\Big]^{\mathrm{T}}, \end{aligned} \tag{A.1}$$

where $\mathbf{T}^{\pm}$ (kg/s^3) are third order distribution function moments with $\mathbf{T}^{+} = \gamma_3 \mathbf{T}^{-}$ and γ_3 (dimensionless) a constant equal to 0.8. The fourth order distribution function moments $\mathbf{F}^{\pm}$ (kg m/s^4) are set equal to zero as they do not affect macroscopic variables. The sub-grid scale stress tensor $\boldsymbol{\tau}_{\mathrm{SGS}}$, relevant for turbulence modelling, is set equal to zero for laminar mixing. The 2nd order velocity moments are given by $\alpha_{5-10}^{\pm}$, and contain components of the strain rate tensor ϵ, defined by Eq. (7). To extract e.g. the 1st component ϵ_{xx}, with $\tau_{\mathrm{SGS},xx} = 0$:

$$\alpha_5^{-} = \rho u_x^2 + \rho\left(\frac{-1 - 6\nu}{6}\right)\left(2\frac{\partial u_x}{\partial x}\right), \tag{A.2}$$

$$\frac{\alpha_5^{-} - \rho u_x^2}{\rho\left(\frac{-1-6\nu}{6}\right)} = 2\frac{\partial u_x}{\partial x} = \epsilon_{xx}, \tag{A.3}$$

$$\epsilon_{xx} = \frac{6\left(\alpha_5^{-} - \rho u_x^2\right)}{\rho(-1 - 6\nu)}; \tag{A.4}$$

thus, ϵ is obtained from $\boldsymbol{\alpha}^{-}$ by the following:

$$\boldsymbol{\epsilon} = \begin{bmatrix} \frac{6\left(\alpha_5^{-} - \rho u_x^2\right)}{\rho(-1-6\nu)} & \frac{6\left(\alpha_6^{-} - \rho u_x u_y\right)}{\rho(-1-6\nu)} & \frac{6\left(\alpha_8^{-} - \rho u_x u_z\right)}{\rho(-1-6\nu)} \\ \frac{6\left(\alpha_6^{-} - \rho u_x u_y\right)}{\rho(-1-6\nu)} & \frac{6\left(\alpha_7^{-} - \rho u_y^2\right)}{\rho(-1-6\nu)} & \frac{6\left(\alpha_9^{-} - \rho u_y u_z\right)}{\rho(-1-6\nu)} \\ \frac{6\left(\alpha_8^{-} - \rho u_x u_z\right)}{\rho(-1-6\nu)} & \frac{6\left(\alpha_9^{-} - \rho u_y u_z\right)}{\rho(-1-6\nu)} & \frac{6\left(\alpha_{10}^{-} - \rho u_z^2\right)}{\rho(-1-6\nu)} \end{bmatrix}. \tag{A.5}$$

Appendix B. Supplementary data

Supplementary material related to this article can be found online at https://doi.org/10.1016/j.cherd.2025.09.025.

References

Alberini, F., Albano, A., Singh, P., Christodoulou, C., Montante, G., Maluta, F., Paglianti, A., 2024. Fluid dynamics and power consumptions in a single use stirred tank adopted in the pharmaceutical industry. Chem. Eng. Res. Des. 204, 159–171. http://dx.doi.org/10.1016/j.cherd.2024.02.023.

ANSYS, Inc., 2022. ANSYS® fluent meshing (2022 R1).

ANSYS, Inc., 2023. ANSYS® fluent (2023 R2).

Antony, J., 2014. Design of experiments for engineers and scientists, second ed. Elsevier Insights, Elsevier, London, http://dx.doi.org/10.1016/C2012-0-03558-2.

Battista, F., Fino, D., Mancini, G., Ruggeri, B., 2016. Mixing in digesters used to treat high viscosity substrates: The case of olive oil production wastes. J. Env. Chem. Eng. 4 (1), 915–923. http://dx.doi.org/10.1016/j.jece.2015.12.032.

Bertrand, J., 1983. Agitation De Fluides Visqueux. Cas De Mobiles À Pales, D'ancres Et De Barrières (Ph.D. thesis). Institut National Polytechnique de Toulouse, Toulouse, France.

Bibeau, V., Barbeau, L., Boffito, D.C., Blais, B., 2023. Artificial neural network to predict the power number of agitated tanks fed by CFD simulations. Can. J. Chem. Eng. 101 (10), 5992–6002. http://dx.doi.org/10.1002/cjce.24870.

Bird, R.B., Stewart, W.E., Lightfoot, E.N., Klingenberg, D.J., 2015. Introductory Transport Phenomena, first ed. Wiley, Hoboken, NJ.

Boston, L.M., 2025. In Silico Optimisation of Viscous Mixing of Shear-Thinning Liquids (Ph.D. thesis). University of Aberdeen, http://dx.doi.org/10.20392/2MP4-CB75.

Box, G.E.P., Hunter, J.S., Hunter, W.G., 2005. Statistics for experimenters: Design, innovation, and discovery, second ed. Wiley Series in Probability and Statistics, Wiley-Interscience, Hoboken, N.J.

Box, G.E.P., Wilson, K.B., 1951. On the experimental attainment of optimum conditions. J. R. Stat. Soc. Ser. B Methodol. 13 (1), 1–38. http://dx.doi.org/10.1111/j.2517-6161.1951.tb00067.x.

Brito-De La Fuente, E., Choplin, L., Tanguy, P., 1997. Mixing with helical ribbon impellers. Chem. Eng. Res. Des. 75 (1), 45–52. http://dx.doi.org/10.1205/026387697523381.

Cai, S., Mao, Z., Wang, Z., Yin, M., Karniadakis, G.E., 2021. Physics-informed neural networks (PINNs) for fluid mechanics: A review. Acta Mech. Sin. 37 (12), 1727–1738. http://dx.doi.org/10.1007/s10409-021-01148-1.

Chen, G., Chen, L., Wang, W., Chen, S., Wang, H., Wei, Y., Hong, F.F., 2019. Improved bacterial nanocellulose production from glucose without the loss of quality by evaluating thirteen agitator configurations at low speed. Microb. Biotechnol. 12 (6), 1387–1402. http://dx.doi.org/10.1111/1751-7915.13477.

Choi, S., Jung, I., Kim, H., Na, J., Lee, J.M., 2022. Physics-informed deep learning for data-driven solutions of computational fluid dynamics. Korean J. Chem. Eng. 39 (3), 515–528. http://dx.doi.org/10.1007/s11814-021-0979-x.

Choong, C.E., Ibrahim, S., El-Shafie, A., 2020. Artificial Neural Network (ANN) model development for predicting just suspension speed in solid-liquid mixing system. Flow Meas. Instrum. 71, 101689. http://dx.doi.org/10.1016/j.flowmeasinst.2019.101689.

Dapelo, D., Kummerländer, A., Krause, M.J., Bridgeman, J., 2023. Lattice-Boltzmann LES modelling of a full-scale, biogas-mixed anaerobic digester. Eng. Comput. http://dx.doi.org/10.1007/s00366-023-01854-3.

Dapelo, D., Trunk, R., Krause, M.J., Bridgeman, J., 2019. Towards Lattice-Boltzmann modelling of unconfined gas mixing in anaerobic digestion. Comput. & Fluids 180, 11–21. http://dx.doi.org/10.1016/j.compfluid.2018.12.008.

Dapelo, D., Trunk, R., Krause, M.J., Cassidy, N., Bridgeman, J., 2020. The application of Buckingham π theorem to Lattice-Boltzmann modelling of sewage sludge digestion. Comput. & Fluids 209, 104632. http://dx.doi.org/10.1016/j.compfluid.2020.104632.

Dassault Systèmes SolidWorks Corporation, 2021. SOLIDWORKS® education edition.

de Waele, A., 1923. Viscometry and plastometry. Oil Colour Chem. Assoc. J. 6, 33–88.

Delaplace, G., Leuliet, J.C., Relandeau, V., 2000a. Circulation and mixing times for helical ribbon impellers. Review and experiments. Exp. Fluids 28 (2), 170–182. http://dx.doi.org/10.1007/s003480050022.

Delaplace, G., Leuliet, J.-C., Ronse, G., 2000b. Power requirement when mixing a shear-thickening fluid with a helical ribbon impeller type. Chem. Eng. Technol. 23 (4), 329–335. http://dx.doi.org/10.1002/(SICI)1521-4125(200004)23:4<329::AID-CEAT329>3.0.CO;2-0.

Derksen, J., 2018. Assessing Eulerian–Lagrangian simulations of dense solid-liquid suspensions settling under gravity. Comput. & Fluids 176, 266–275. http://dx.doi.org/10.1016/j.compfluid.2016.12.017.

Derksen, J., Van den Akker, H.E.A., 1999. Large eddy simulations on the flow driven by a Rushton turbine. AIChE J. 45 (2), 209–221. http://dx.doi.org/10.1002/aic.690450202.

Derringer, G., 1994. A balancing act: Optimizing a product's properties. Qual. Prog. 27 (6), 51–58.

Derringer, G., Suich, R., 1980. Simultaneous optimization of several response variables. J. Qual. Technol. 12 (4), 214–219. http://dx.doi.org/10.1080/00224065.1980.11980968.

Eggels, J., Somers, J., 1995. Numerical simulation of free convective flow using the Lattice-Boltzmann scheme. Int. J. Heat Fluid Flow 16 (5), 357–364. http://dx.doi.org/10.1016/0142-727X(95)00052-R.

Eibl, P., Rustige, S., Witz, C., Khinast, J., 2020. LBM for two-phase (bio-)reactors. In: Advances in Chemical Engineering. Vol. 55, Elsevier, pp. 219–285. http://dx.doi.org/10.1016/bs.ache.2020.04.003.

Ford, C., Ein-Mozaffari, F., Bennington, C.P.J., Taghipour, F., 2006. Simulation of mixing dynamics in agitated pulp stock chests using CFD. AIChE J. 52 (10), 3562–3569. http://dx.doi.org/10.1002/aic.10958.

Fortunato, V.A., Caneppele, F.L., Ribeiro, R., Rabi, J.A., 2018. Development of in-house lattice-Boltzmann simulator of bioreactors for wastewater treatment: Basic concepts and initial results. Water Sci. Technol. 77 (3), 838–847. http://dx.doi.org/10.2166/wst.2017.597.

Frank, M., Wolfe, P., 1956. An algorithm for quadratic programming. Nav. Res. Logist. Q. 3 (1–2), 95–110. http://dx.doi.org/10.1002/nav.3800030109.

Goldstein, D., Handler, R., Sirovich, L., 1993. Modeling a no-slip flow boundary with an external force field. J. Comput. Phys. 105 (2), 354–366. http://dx.doi.org/10.1006/jcph.1993.1081.

Grenville, R.K., Nienow, A.W., 2003. Blending of miscible liquids. In: Paul, E.L., Atiemo-Obeng, V.A., Kresta, S.M. (Eds.), Handbook of Industrial Mixing, first ed. Wiley, pp. 507–542. http://dx.doi.org/10.1002/0471451452.ch9.

Guadarrama-Pérez, R., Márquez-Baños, V.E., De La Concha-Gómez, A.D., Valencia-López, J.J., Vengoechea-Pimienta, A., Martínez De Jesús, G., Ramírez-Muñoz, J., 2020. Hydrodynamic performance of a ring-style high-shear impeller in Newtonian and shear-thinning fluids. Chem. Eng. Technol. 43 (11), 2325–2335. http://dx.doi.org/10.1002/ceat.201900569.

Hemrajani, R.R., Tatterson, G.B., 2003. Mechanically stirred vessels. In: Paul, E.L., Atiemo-Obeng, V.A., Kresta, S.M. (Eds.), Handbook of Industrial Mixing, first ed. Wiley, pp. 345–390. http://dx.doi.org/10.1002/0471451452.ch6.

Huang, Y., MahmoodPoor Dehkordy, F., Li, Y., Emadi, S., Bagtzoglou, A., Li, B., 2018. Enhancing anaerobic fermentation performance through eccentrically stirred mixing: Experimental and modeling methodology. Chem. Eng. J. 334, 1383–1391. http://dx.doi.org/10.1016/j.cej.2017.11.088.

Hurvich, C.M., Tsai, C.-L., 1989. Regression and time series model selection in small samples. Biom. 76 (2), 297–307. http://dx.doi.org/10.1093/biomet/76.2.297.

Jones, B., Nachtsheim, C.J., 2013. Definitive screening designs with added two-level categorical factors. J. Qual. Technol. 45 (2), 121–129. http://dx.doi.org/10.1080/00224065.2013.11917921.

Kang, Z., Feng, L., Wang, J., 2024. Optimization of a gas–liquid dual-impeller stirred tank based on deep learning with a small data set from CFD simulation. Ind. Eng. Chem. Res. 63 (1), 843–855. http://dx.doi.org/10.1021/acs.iecr.3c03561.

Karim, K., Varma, R., Vesvikar, M., Al-Dahhan, M., 2004. Flow pattern visualization of a simulated digester. Water Res. 38 (17), 3659–3670. http://dx.doi.org/10.1016/j.watres.2004.06.009.

Krüger, T., Kusumaatmaja, H., Kuzmin, A., Shardt, O., Silva, G., Viggen, E.M., 2017. The Lattice Boltzmann method: Principles and practice, first ed. Graduate Texts in Physics, Springer International Publishing, Cham, http://dx.doi.org/10.1007/978-3-319-44649-3.

Kummerländer, A., Bingert, T., Bukreev, F., Czelusniak, L.E., Dapelo, D., Hafen, N., Heinzelmann, M., Ito, S., Jeßberger, J., Kusumaatmaja, H., Marquardt, J.E., Rennick, M., Pertzel, T., Prinz, F., Sadric, M., Schecher, M., Simonis, S., Sitter, P., Teutscher, D., Zhong, M., Krause, M.J., 2024. OpenLB Release 1.7: Open Source Lattice Boltzmann Code. Zenodo, http://dx.doi.org/10.5281/ZENODO.10684609.

Landry, H., Laguë, C., Roberge, M., 2004. Physical and rheological properties of manure products. Appl. Eng. Agric. 20 (3), 277–288. http://dx.doi.org/10.13031/2013.16061.

Lasdon, L.S., Waren, A.D., Jain, A., Ratner, M., 1978. Design and testing of a generalized reduced gradient code for nonlinear programming. ACM Trans. Math. Software 4 (1), 34–50. http://dx.doi.org/10.1145/355769.355773.

Lebranchu, A., Delaunay, S., Marchal, P., Blanchard, F., Pacaud, S., Fick, M., Olmos, E., 2017. Impact of shear stress and impeller design on the production of biogas in anaerobic digesters. Bioresour. Technol. 245, 1139–1147. http://dx.doi.org/10.1016/j.biortech.2017.07.113.

Li, H., Sansalone, J., 2022. A CFD-ML augmented alternative to residence time for clarification basin scaling and design. Water Res. 209, 117965. http://dx.doi.org/10.1016/j.watres.2021.117965.

López-Jiménez, P.A., Escudero-González, J., Montoya Martínez, T., Fajardo Montañana, V., Gualtieri, C., 2015. Application of CFD methods to an anaerobic digester: The case of ontinyent WWTP, Valencia, Spain. J. Water Process. Eng. 7, 131–140. http://dx.doi.org/10.1016/j.jwpe.2015.05.006.

Mao, L., Tsui, T.-H., Zhang, J., Dai, Y., Tong, Y.W., 2021. Mixing effects on decentralized high-solid digester for horticultural waste: Startup, operation and sensitive microorganisms. Bioresour. Technol. 333, 125216. http://dx.doi.org/10.1016/j.biortech.2021.125216.

McKay, M.D., Beckman, R.J., Conover, W.J., 1979. A comparison of three methods for selecting values of input variables in the analysis of output from a computer code. Technometrics 21 (2), 239. http://dx.doi.org/10.2307/1268522, arXiv:1268522.

Meister, M., Rezavand, M., Ebner, C., Pümpel, T., Rauch, W., 2018. Mixing non-Newtonian flows in anaerobic digesters by impellers and pumped recirculation. Adv. Eng. Softw. 115, 194–203. http://dx.doi.org/10.1016/j.advengsoft.2017.09.015.

Metzner, A.B., Otto, R.E., 1957. Agitation of non-Newtonian fluids. AIChE J. 3 (1), 3–10. http://dx.doi.org/10.1002/aic.690030103.

Mihailova, O., Mothersdale, T., Rodgers, T., Ren, Z., Watson, S., Lister, V., Kowalski, A., 2018. Optimisation of mixing performance of helical ribbon mixers for high throughput applications using computational fluid dynamics. Chem. Eng. Res. Des. 132, 942–953. http://dx.doi.org/10.1016/j.cherd.2018.01.053.

Minitab, LLC., 2021. Minitab® (20.3).

Mokhefi, A., Bouanini, M., Elmir, M., Guettaf, Y., Spiteri, P., 2022. Numerical investigation of mixed convection in an anchor-stirred tank filled with an Al2O3-water nanofluid. Chem. Pap. 76 (2), 967–985. http://dx.doi.org/10.1007/s11696-021-01914-2.

Montgomery, D.C., 2019. Design and Analysis of Experiments, tenth ed. Wiley, Hoboken, NJ.

Neuner, T., Meister, M., Pillei, M., Rauch, W., 2024. Optimizing mixing efficiency of anaerobic digesters with high total solids concentrations using validated CFD simulations. Biochem. Eng. J. 208, 109320. http://dx.doi.org/10.1016/j.bej.2024.109320.

Ostwald, W., 1925. Ueber die Geschwindigkeitsfunktion der Viskosität disperser Systeme. I. Kolloid-Z. 36 (2), 99–117. http://dx.doi.org/10.1007/BF01431449.

Patterson, W.I., Carreau, P.J., Yap, C.Y., 1979. Mixing with helical ribbon agitators: Part II. Newtonian Fluids. AIChE J. 25 (3), 508–516. http://dx.doi.org/10.1002/aic.690250317.

Paul, E.L., Atiemo-Obeng, V.A., Kresta, S.M. (Eds.), 2003. Handbook of Industrial Mixing, first ed. John Wiley & Sons, Inc., Hoboken, NJ, USA, http://dx.doi.org/10.1002/0471451452.

Prajapati, P., Ein-Mozaffari, F., 2009. CFD investigation of the mixing of yield-pseudoplastic fluids with anchor impellers. Chem. Eng. Technol. 32 (8), 1211–1218. http://dx.doi.org/10.1002/ceat.200800511.

Rahimzadeh, A., Ranjbarrad, S., Ein-Mozaffari, F., Lohi, A., 2024. Application of machine learning models in coaxial bioreactors: classification and torque prediction. ChemEngineering 8 (2), 42. http://dx.doi.org/10.3390/chemengineering8020042.

Ramírez-Muñoz, J., Guadarrama-Pérez, R., Márquez-Baños, V., 2017. A direct calculation method of the Metzner-Otto constant by using computational fluid dynamics. Chem. Eng. Sci. 174, 347–353. http://dx.doi.org/10.1016/j.ces.2017.09.023.

Rao, S.S., 2019. Engineering Optimization Theory and Practice, fifth ed. Wiley, http://dx.doi.org/10.1002/9781119454816.

Rezavand, M., Winkler, D., Sappl, J., Seiler, L., Meister, M., Rauch, W., 2019. A fully Lagrangian computational model for the integration of mixing and biochemical reactions in anaerobic digestion. Comput. & Fluids 181, 224–235. http://dx.doi.org/10.1016/j.compfluid.2019.01.024.

Rieger, F., Novák, V., Havelková, D., 1988. The influence of the geometrical shape on the power requirement of ribbon impellers. Int. Chem. Eng. 28 (2), 376–383.

Robinson, M., Cleary, P.W., 2012. Flow and mixing performance in helical ribbon mixers. Chem. Eng. Sci. 84, 382–398. http://dx.doi.org/10.1016/j.ces.2012.08.044.

Rushton, J.H., Costich, E.W., Everett, H.J., 1950. Power characteristics of mixing impellers part II. Chem. Eng. Prog. 46 (9), 467–476.

Shamlou, P., Edwards, M., 1985. Power consumption of helical ribbon mixers in viscous Newtonian and non-Newtonian fluids. Chem. Eng. Sci. 40 (9), 1773–1781. http://dx.doi.org/10.1016/0009-2509(85)80040-3.

Shamlou, P., Edwards, M., 1989. Power consumption of anchor impellers in Newtonian and non-Newtonian liquids. Chem. Eng. Res. Des. 67, 537–543.

Shekhar, S.M., Jayanti, S., 2003. Mixing of power-law fluids using anchors: Metzner-Otto concept revisited. AIChE J. 49 (1), 30–40. http://dx.doi.org/10.1002/aic.690490105.

Siemens Digital Industries Software, 2021a. HEEDS.

Siemens Digital Industries Software, 2021b. Simcentre STAR-CCM+.

Singh, B., Kovács, K.L., Bagi, Z., Nyári, J., Szepesi, G.L., Petrik, M., Siménfalvi, Z., Szamosi, Z., 2021. Enhancing efficiency of anaerobic digestion by optimization of mixing regimes using helical ribbon impeller. Ferment. 7 (4), 251. http://dx.doi.org/10.3390/fermentation7040251.

Singh, B., Szamosi, Z., Siménfalvi, Z., 2019. State of the art on mixing in an anaerobic digester: A review. Renew. Energy 141, 922–936. http://dx.doi.org/10.1016/j.renene.2019.04.072.

Soheel, A.H., Faraj, J.J., Hussien, F.M., 2023. CFD analysis for anaerobic digestion inside a batch digester augmented with extended surfaces. Front. Heat Mass Transf. 20, http://dx.doi.org/10.5098/hmt.20.3.

Somers, J.A., 1993. Direct simulation of fluid flow with cellular automata and the Lattice-Boltzmann equation. Appl. Sci. Res. 51 (1–2), 127–133. http://dx.doi.org/10.1007/BF01082526.

ten Cate, A., Nieuwstad, C.H., Derksen, J.J., Van den Akker, H.E.A., 2002. Particle imaging velocimetry experiments and Lattice-Boltzmann simulations on a single sphere settling under gravity. Phys. Fluids 14 (11), 4012–4025. http://dx.doi.org/10.1063/1.1512918.

Tobo, Y.M., Rehman, U., Bartacek, J., Nopens, I., 2020. Partial integration of ADM1 into CFD: Understanding the impact of diffusion on anaerobic digestion mixing. Water Sci. Technol. 81 (8), 1658–1667. http://dx.doi.org/10.2166/wst.2020.076.

Tsui, Y.-Y., Hu, Y.-C., 2011. Flow characteristics in mixers agitated by Helical Ribbon Blade Impeller. Eng. Appl. Comput. Fluid Mech. 5 (3), 416–429. http://dx.doi.org/10.1080/19942060.2011.11015383.

Vesvikar, M., Varma, R., Karim, K., Al-Dahhan, M., 2005. Flow pattern visualization in a mimic anaerobic digester: Experimental and computational studies. Water Sci. Technol. 52 (1–2), 537–543. http://dx.doi.org/10.2166/wst.2005.0564.

Wang, H., Chaffart, D., Ricardez-Sandoval, L.A., 2019. Modelling and optimization of a pilot-scale entrained-flow gasifier using artificial neural networks. Energy 188, 116076. http://dx.doi.org/10.1016/j.energy.2019.116076.

Wu, B., 2012. CFD simulation of mixing for high-solids anaerobic digestion. Biotechnol. Bioeng. 109 (8), 2116–2126. http://dx.doi.org/10.1002/bit.24482.

Wu, M., Jurtz, N., Walle, A., Kraume, M., 2022. Evaluation and application of efficient CFD-based methods for the multi-objective optimization of stirred tanks. Chem. Eng. Sci. 263, 118109. http://dx.doi.org/10.1016/j.ces.2022.118109.

Xiao, W., Zhang, H., Luo, K., Mao, C., Fan, J., 2020. Immersed boundary method for multiphase transport phenomena. Rev. Chem. Eng. 38 (4), 363–405. http://dx.doi.org/10.1515/revce-2019-0076.

Yao, Z., Xu, H., Li, J., Xu, T., 2023. Multi-objective optimization of stirring tank based on multiphase flow simulation. Chem. Eng. Res. Des. 189, 680–693. http://dx.doi.org/10.1016/j.cherd.2022.11.043.

Zhang, Y., Peterson, E.C., Ng, Y.L., Goh, K.-L., Zivkovic, V., Chow, Y., 2023. Comparison of Raspberry ketone production via submerged fermentation in different bioreactors. Ferment. 9 (6), 546. http://dx.doi.org/10.3390/fermentation9060546.

Zhao, X., Fan, H., Lin, G., Fang, Z., Yang, W., Li, M., Wang, J., Lu, X., Li, B., Wu, K.-J., Fu, J., 2024. Multi-objective optimization of radially stirred tank based on CFD and machine learning. AIChE J. 70 (3), e18324. http://dx.doi.org/10.1002/aic.18324.